A mechanistic model for the complex conductivity of clay materials. II. Comparison to experimental data

Alexis Maineult, Philippe Leroy, Aida Mendieta, Damien Jougnot

A mechanistic model for the complex conductivity of clay materials. II. Comparison to experimental data

Alexis Maineult[1], Philippe Leroy[2,*], Aida Mendieta[3], Damien Jougnot[4]

[1] Laboratoire de Géologie, Ecole Normale Supérieure / CNRS UMR8538, PSL Research University, 75005 Paris, France.

[2] BRGM, French Geological Survey, 45060 Orléans, France.

[3] Université de Paris, Institut de Physique du Globe de Paris, CNRS, 75005 Paris, France.

[4] Sorbonne Université, CNRS, EPHE, UMR 7619 METIS, 75005 Paris, France.

[*]Corresponding author, p.leroy@brgm.fr

Intended for publication in Geophysical Journal International

SUMMARY

Clays are very abundant minerals in the Earth's crust and express a high conductivity response that can be observed at the scale of the geological formation by electrical and electromagnetic methods. However, these minerals have a complex microstructure that renders difficult the quantitative petrophysical interpretation of the electrical field measurements. In this study, we developed a new approach to interpret spectral induced polarisation (SIP) signals measured on clay materials in terms of microstructural and electrical double layer (EDL) properties, including surface conductivity, using the physical model recently developed by Leroy *et al.* (2024). With a restrained set of optimised physical-chemical parameters, i.e., the fraction of the counter-charge and cation effective ion mobility in the Stern layer, number of stacked sheets per montmorillonite particle, and clay aggregate

effective shape and size distribution, our model well reproduces the measured laboratory SIP spectra in the mHz to kHz frequency range on kaolinite, illite and montmorillonite muds at different NaCl concentrations. Our results suggest that most of the EDL counter-charge controlling SIP spectra is located in the Stern layer on the basal surfaces. First Archie's law explains the in-phase conductivity measurements provided that the contribution of the diffuse layer to water conductivity is properly included. The ratio of imaginary surface conductivity to real surface conductivity is highly dependent on frequency and slightly dependent on salinity. Finally the measured quadrature conductivity is proportional but not necessarily equal to the imaginary surface conductivity. Our study is a step forward to better understand the complex electrical conductivity of clays.

Key words: Electrical properties, Induced polarisation, Microstructure.

1 INTRODUCTION

Clays are fined-grained materials (with particle size below 2 μm) having a very high specific surface area (SSA) (Grim 1962). One gram of clay mineral can cover a surface typically comprised between 10 and 1000 m^2 (see the review in Revil & Leroy 2004). Montmorillonite clay, with a SSA of about 800 m^2 g^{-1}, has the highest known SSA among major natural minerals (Tournassat *et al.* 2015). Clay minerals are very common in the Earth's crust, especially in geologic deposits, terrestrial weathering environments like regolith, and marine sediments (Thiry 2000). They are the main constituent of soils and extended sedimentary stratigraphic layers (Schroeder 2018). For instance, illite and smectite alone constitute about 30 % of all sedimentary rocks on Earth (Garrels & Mackenzie 1971) and extra-terrestrial smectite was even observed by the Curiosity rover on Mars (Bristow *et al.* 2018).

Clay particles have a unique lamellar microstructure (e.g., Sposito 1989). They are hydrous layer aluminosilicates made by a stack of octahedral (O) alumina sheet sandwiched between two tetrahedral (T) silica sheets (e.g., montmorillonite and illite particles) or of tetrahedral silica and octahedral alumina sheets (e.g., kaolinite particles) (Grim 1962). Phyllosilicate clay minerals have a broad range of specific surface areas, from typically 10-20 $m^2\ g^{-1}$ (chlorite and kaolinite), 100-200 $m^2\ g^{-1}$ (illite) to 700-800 $m^2\ g^{-1}$ (montmorillonite) (e.g., Tournassat *et al.* 2003; Revil & Leroy 2004; Hassan *et al.* 2006; Tournassat *et al.* 2015). Clays are also characterized by a high negative surface charge when in contact with water, in particular when isomorphic substitutions (replacement of Si^{4+} by Al^{3+} or Fe^{3+} ions in tetrahedral sheets and of Al^{3+} by Mg^{2+} or Fe^{2+} ions in octahedral sheets) occur in, e.g., illite and montmorillonite crystals (García-Romero *et al.* 2021). For instance, the surface charge density of hydrated montmorillonite is typically between -0.15 and -0.1 C m^{-2} (Tournassat *et al.* 2011).

High specific surface area and negative surface charge are responsible for the high measured cation exchange capacity (CEC) of clays, typically between 0.1 and 1.5 meq g^{-1} (Bergaya & Vayer 1997), which confer them remarkable adsorption properties (Tournassat *et al.* 2011). High specific surface area and negative surface charge of clays are also responsible for the very low permeability of clay materials (clay geologic formations have permeability values typically between 10^{-23} and 10^{-17} m^2 (Neuzil 1994)). Compacted clay rocks such as argillites have a very low permeability at saturation, typically around 10^{-21} m^2 (Jougnot *et al.* 2010a), because their pores contain a significant content of nanopores filled by the electrical double layer (EDL) surrounding the clay mineral surface in contact with water and compensating the usual negative surface charge of the mineral (Leroy et *al.* 2007).

Materials containing clays are used in many geo-environmental and engineering applications (see for example the references inside Leroy *et al.* (2017) and Ural (2018) in geotechnics). For instance, clay membrane barriers (natural and synthetic clays) adsorb salt ions (Ali *et al.*

2021), metallic pollutants (Gehin *et al.* 2007) and organic pollutants (Kausar *et al.* 2018) and hence are used to improve water quality (Ewis *et al.* 2022). In absence of connected fractures and of the significant presence of more permeable minerals than clays, ion diffusion over geological time scale is the main transport process through clay materials (Rotenberg *et al.* 2007). Clay geological formations (e.g., marls, shale, mudstone, argillite and claystone), because of their confining properties, serve as cap rocks above green (or de-carbonated) energies (e.g., from stored H_2 as an energy vector, and geothermal energy (Guisseau *et al.* 2007)) and carbonated energies (e.g., from oil and gas (Li *et al.* 2006)). Clay rocks such as argillites are used for the geological storage of high-level nuclear waste (Yven *et al.* 2007) and CO_2 (Tao *et al.* 2022). Clay membrane barriers, e.g., swelling bentonites, develop plasticity when wet and act as containers of industrial and domestic wastes (Malusis *et al.* 2003), and are also used for the geological storage of high-level nuclear waste (Leroy *et al.* 2006). The presence of swelling clays in the soil and underground can also induce adverse effects. For instance, the swelling of smectites due to clay hydration results to quick clay landslides and the shrinkage of smectites due to clay dehydration can fracture buildings, an issue or paramount importance in civil engineering (Khaldoun *et al.* 2009). The swelling of smectites also complicates subsurface oil and gas extraction (Anderson *et al.* 2010).

Clays in contact with water express a high excess of electrical conductivity on their surface because of the large number of moving counter-ions in the EDL (Obrien & Rowlands 1993; Rasmusson *et al.* 1997; Revil & Leroy 2001; Leroy & Revil 2004). In geophysics, electrical methods (e.g., Revil *et al.* 2005) and electromagnetic methods (e.g., Porté *et al.* 2023), typically undertaken on the ground surface or in boreholes, are very sensitive to the high conductivity of clays. These methods, used conjointly with geochemical and hydrogeological methods (e.g., using physico-chemical analyses and reactive transport modelling), can map in real-time and in 2 or 3 dimensions the state (e.g., water content, clay content, salinity) and

transport properties (e.g., diffusive transport, permeability) and fluid and mineralogical distributions of geological formations (e.g., Kemna *et al.* 2012; Binley *et al.* 2015; Peshtani *et al.* 2024).

Among electrical and electromagnetic methods in geophysics, spectral induced polarisation (SIP) is based on the injection of a low-frequency (typically from mHz to kHz) sinusoidal electrical current through the investigated medium and to the measurement of the resulting voltage (Pelton *et al.* 1978). The measured voltage magnitude and phase-shift between injected current and measured voltage give access to the complex conductivity of the investigated medium, i.e. to the imaginary part of the complex conductivity of the investigated medium in addition to the real part traditionally inferred from electrical resistivity tomography (ERT) (e.g., Jougnot *et al.* 2010b; Binley *et al.* 2015). Under the influence of the applied low-frequency electrical field, ions in the EDL electromigrate, polarise the EDL surrounding the clay minerals and diffuse back to their equilibrium position, increasing both conductivity magnitude and phase-shift or real and imaginary conductivity measurements (de Lima & Sharma 1992).Clays have a complex microstructure (e.g., Massat et *al.* 2016; Chaaya *et al.* 2023) and their high conductivity response (notably the contributions from the clay particle surface and the pore water) is actually not completely understood in geophysics because most petrophysical SIP models (e.g., Vinegar & Waxman 1984; Börner *et al.* 1993; Weller *et al.* 2013) do not consider explicitly clay microstructure and EDL properties that are established at the nanometric scale (Okay *et al.* 2014; Qi & Wu 2022, 2024). Indeed, these petrophysical models are not mechanistic ones because they are not based on ionic transport equations (like Poisson-Nernst-Planck equations, see for example Bücker *et al.* 2019). They are established at the scale of the representative elementary volume (REV) that is much larger than the scale of clay particles (de Lima & Sharma 1992). They are based on phenomenological equivalent circuit models that consider water conduction

(resistor) in parallel with surface conduction (a resistor in series with a capacitor for taking into account polarisation). In addition, the diffuse layer of thin clay particles such as illite and montmorillonite particles can be larger than the particle thickness hence not contributing to particle surface conductivity as defined by O'Konski (1960) (Leroy & Revil 2009; Leroy et *al.* 2017). In addition, Na-montmorillonite particle contains hydrated and mobile Na^+ ions in the interlayer space between TOT sheets (e.g., Bourg *et al.* 2003; Tournassat & Steefel 2019) that can contribute to the measured high electrical conductivity response (e.g., Rotenberg *et al.* 2005; Greathouse *et al.* 2016).

In this work, we use the mechanistic SIP model recently developed in a companion paper by Leroy *et al.* (2024), which explicitly considers clay microstructural and electrochemical properties, to understand the SIP measurements by Mendieta *et al.* (2021) on kaolinite, illite and montmorillonite mud samples at different NaCl concentrations. Mud porosity, electrical formation factor, water conductivity and clay surface conductivity as well as aggregate size distributions are extracted from the comparison of the model to the measurements. Section 2 of our manuscript presents the model and the optimisation procedure used to determine the best values of the parameters. Section 3 shows the comparison of the predictions to the experimental data and a discussion including a comparison to the petrophysical model by Weller *et al.* (2013) for clayey materials.

2 SIP MODEL AND OPTIMIZATION PROCEDURE

2.1 Methodology

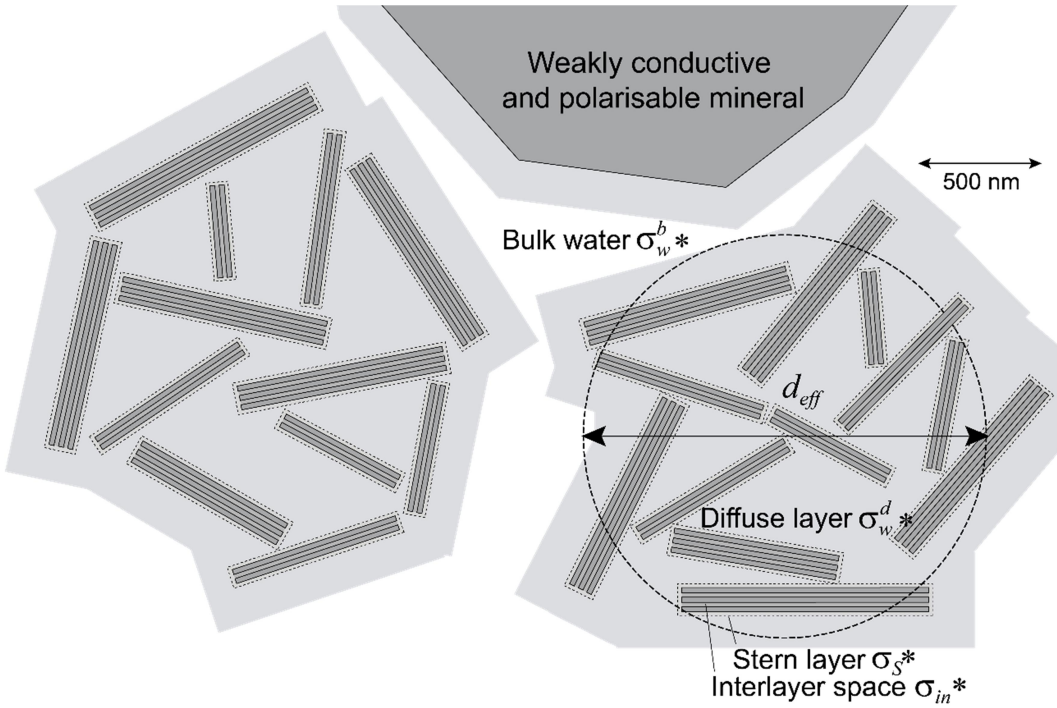

Figure 1. Sketch of a clay mud containing montmorillonite aggregates with an effective diameter d_{eff} showing the clay particles interacting with each other and the electrical conductivities of the different components of the aggregate (not to scale) (modified from Leroy *et al.* 2024).

A wet clay mud contains clay particles that are interacting each other to form aggregates (Coussot & Piau 1994). The EDL of clays is typically made of a "compact" Stern layer with a solid-like viscosity and containing mostly counter-ions and of a diffuse layer with a liquid-like viscosity and containing an excess of counter-ions and a deficiency of co-ions (Tournassat *et al.* 2009). We assume that the Stern layer and the interlayer space (in the case of Na-montmorillonite) as well as the diffuse layer and the bulk water (not influenced by clay surface charge) contribute to the electrical conductivity of the mud (Fig. 1). In addition, in our model, displacement current is considered in addition to conduction current (for more related information read section 3 of Leroy *et al.* 2024), as indicated by the asterisks on the right side

of the sigma symbols in Fig. 1. The diffuse layer (like bulk water) is assumed to contribute to water (volume) conductivity and not to the surface conductivity of the particle because the diffuse layer can be thicker than the particle (the thickness of a TOT platelet of sodic montmorillonite (Na-Mt) is ~9.5 Å (Tournassat *et al.* 2015), see related discussion in section 2 of Leroy *et al.* 2024). The mobile counter-ions in the Stern layer around clay particles and in the interlayer space of Na-Mt particles are assumed to be responsible for the surface conductivity of the interacting clay particles within clay aggregates controlling low-frequency polarisation (Leroy *et al.* 2017; Leroy *et al.* 2024). In the case of Na-Mt, our model assumes that the interlayer space behaves like an EDL where water molecules have smaller permittivity than in the bulk water and the diffuse layer (for more related information read section 2.2.1 and section 3.2 of Leroy *et al.* 2024). The model considers the influence of minerals less conductive and polarisable than the main clay mineral like quartz, feldspars or carbonates on the modelled complex conductivity by considering them not conductive and polarisable compared to the main clay mineral. Finally, Maxwell-Wagner polarisation is simulated from the computed complex conductivities of the liquid and solid components of the mud using the self-consistent model of Bruggeman-Hanai-Sen (BHS) (Mendelson & Cohen 1982).

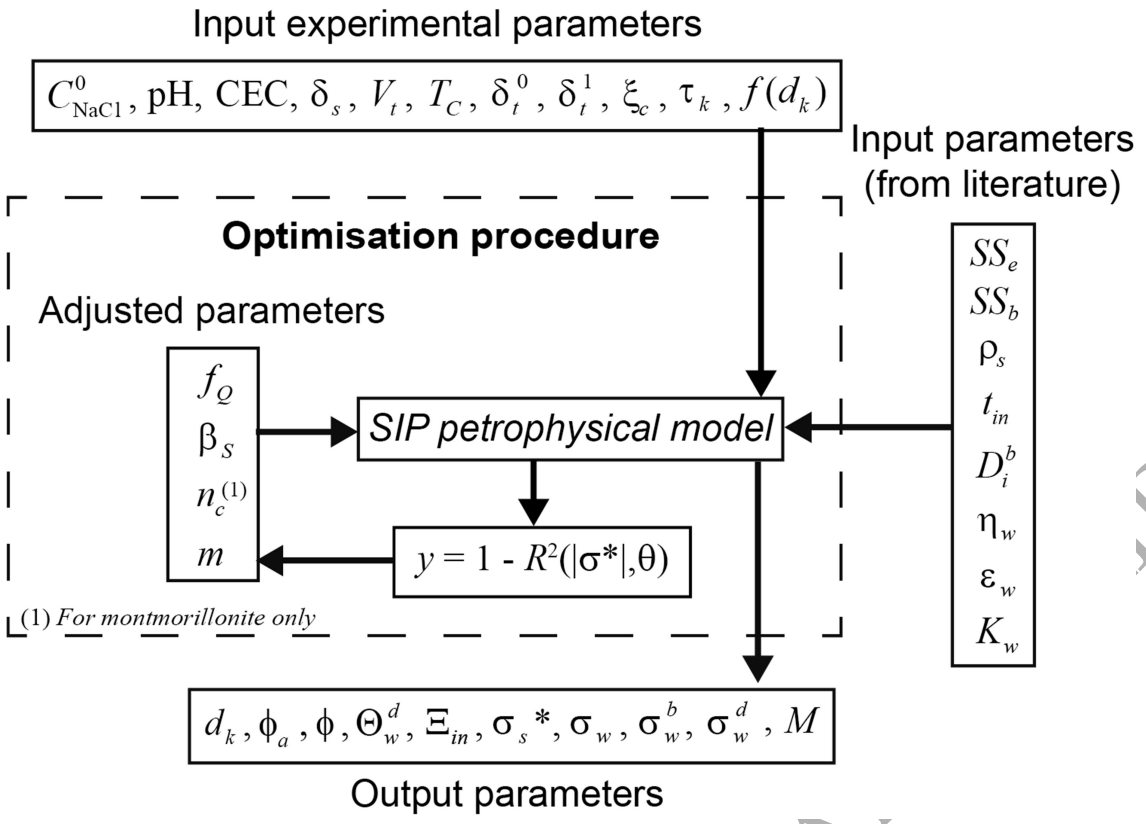

Figure 2. Sketch showing the input and output parameters of the SIP model (explained here including in Tables 2 and 3 and in Leroy *et al.* 2024) and of the optimisation procedure versus the SIP measurements reported in Mendieta *et al.* (2021).

The SIP model is a mechanistic model based on the Nernst-Planck equations for ion electro-migration and back diffusion coupled to the Stokes equations for the effect of water flow (electroosmosis) and to the Laplace and Poisson-Boltzmann equations for the ion distribution in the EDL (Leroy *et al.* 2024). It considers explicitly clay microstructure and electrochemical properties. It has been developed to understand the complex conductivity measurements on clay materials and to extract from them their petrophysical properties (porosity, aggregate size distribution) and geophysical properties (surface conductivity, water conductivity, electrical formation factor) that can be used to estimate material transport properties (ion diffusivity, permeability) (e.g., Jougnot *et al.* 2010b; Peshtani *et al.* 2024).

Some input parameters of the model are from the measured experimental conditions in the

laboratory that are: the initial salt -here NaCl concentration in bulk water (before evaporation, see Mendieta *et al.* 2021) (C^0_{NaCl}), pH of bulk water, cation exchange capacity (CEC), dry clay powder mass (δ_s), sample volume (V_t), temperature in degree Celsius (T_C), sample masses before (δ_t^0), and after evaporation (δ_t^1), and volume fraction of the main clay mineral in the solid phase (ξ_c) (Fig. 2 and Table 1) (Mendieta *et al.* 2021).

Table 1. Experimental input parameters of the SIP model.

Clays	Kaolinite		Illite		Green Mt		Red Mt		
C^0_{NaCl} (M)	0.01	0.1	0.01	0.1	0.01	0.1	0.01	0.1	1
δ_s (g)	373	374	404	438	267	260	350	325	324
V_t (cm^3)	331	331	338	338	329	329	334	334	334
T (°C)	21.8	16.9	21.9	16.4	20.6	16	21.6	16.9	21.6
δ_t^0 (g)	409	604	406	505	690	666	505	502	1003
δ_t^1 (g)	266	317	225	278	452	457	296	326	665

Table 2 presents the input parameters of the SIP model. All computations were carried out using Matlab R2019. The value of D_i^b is taken from measured ion self-diffusion coefficients in distilled water at a temperature of 298.15 K (e.g., $D^b_{\mathrm{Na^+}}(298) = 1.33$ m^2 s^{-1} and $D^b_{\mathrm{Cl^-}}(298) = 2.03$ m^2 s^{-1}) and considers the effect of temperature increasing D_i^b and of salinity decreasing D_i^b for Na^+ and Cl^- ions here (Leroy *et al.* 2015). More details on the input parameters are given in Leroy *et al.* 2024. The aggregate size distribution $f(d_k)$, $k = 1 \ldots L$ (L being the number of different sized aggregates), was computed prior to the optimisation procedure using the method outlined in Leroy *et al.* (2017) based on the calculation of the partial chargeability m_k, i.e., $f(d_k) = m_k / \sum_{k=1}^{L} m_k$ (cf. Appendix A for the computation of the m_k).

For each complex conductivity spectrum, three parameters (case of kaolinite and illite) or four

parameters (case of montmorillonite) were optimised: the fraction of the EDL surface charge density contributing to polarisation (f_Q , $0 \le f_Q \le 1$), the effective ion mobility along the mineral surface of the counter-ions contributing to electrochemical polarisation (β_S), the number of stacked sheets per clay particle (n_c , for montmorillonite only), and the cementation exponent characterizing the shape of the clay aggregates (m) (in theory, $1.2 \le m \le 4$ (Mendelson & Cohen 1982)). We assume that the partition coefficient f_Q corresponds to the fraction of the mineral surface charge density compensated by the Stern layer. The β_S quantity was adjusted by matching simulated to measured SIP spectra using an ion mobility ratio between sodium ion mobility in the Stern layer and in bulk and distilled water at a temperature T of 298 K, $mr_S = \beta_S(298) / \overline{\beta}^b_{\mathrm{Na}^+}(298)$ with $0 \le mr_S \le 1$.

Table 2. Symbols, definitions and units of the input parameters of the SIP model.

Symbol	Definition	Unit
C^0_{NaCl}	initial NaCl concentration in bulk water	mol L^{-1} (M)
pH	potential of hydrogen ion in bulk water	dimensionless
CEC	cation exchange capacity	meq g^{-1}
δ_s	clay powder mass	g
V_t	sample volume	cm^3
T_C	temperature	°C
δ^0_t	sample mass before evaporation	g
δ^1_t	sample mass after evaporation	g
ξ_c	solid volume fraction of the main clay mineral	dimensionless
τ_k (1)	relaxation time of the k^{th} sized aggregate	s
$f(d_k)$ (1)	aggregate size distribution	dimensionless
f_Q (2)	fraction of the EDL surface charge that polarises	dimensionless
β_S (2)	mobility of the counter-ions contributing to polarisation	$m^2\ s^{-1}\ V^{-1}$
n_c (2)	number of stacked sheets per particle	dimensionless
m (2)	cementation exponent of the clay aggregate	dimensionless
SS_e	specific surface area of the edge surfaces	$m^2\ g^{-1}$
SS_b	specific surface area of the basal surfaces	$m^2\ g^{-1}$

ρ_s	solid volumetric mass density	kg m^{-3}
t_{in}	interlayer thickness	m
D_i^b	ion self-diffusion coefficient	m^2 s^{-1}
η_w	liquid water dynamic viscosity	Pa s
ε_w	liquid water dielectric permittivity	F m^{-1}
K_w	dissociation constant of water molecules	dimensionless
M	effect of the diffuse layer on Stern layer polarisation	dimensionless

(1) Parameter value a priori optimised by inverting the relaxation time distribution $f(\tau_k)$.
(2) Parameter value optimised by comparing model predictions to measurements.

The number of TOT ("T" means tetrahedral and "O" means octahedral) sheets per montmorillonite particle (n_c) was adjusted by matching computed to measured SIP spectra in the range 1 to 10 (Leroy *et al.* 2024) as long as clay coagulation does not occur. Otherwise n_c can increase to values typically between 10 and 150 for electrolytes containing Na^+ as dominant cation (Michot *et al.* 2013; Leroy *et al.* 2015).

We did not consider pH changes due to H^+ or OH^- ions or ions released from the interlayer space of montmorillonite or mineral dissolution. Indeed, the initial lowest NaCl concentration in bulk water was relatively high ($C^0_{\mathrm{NaCl}} \cong 10^{-2}$ M), making Na^+ and Cl^- ions the dominant ion species in bulk water during the SIP measurements of Mendieta *et al.* (2021). As a consequence, the pH was fixed to 7 in our computations.

For the fitting procedure of the complex conductivity, we first applied a simulated annealing method (see for instance Maineult 2016), and then we refined the solution using the simplex method (function *fminsearch* in Matlab®). The following cost-function was minimized:

$$y = 1 - R^2 = \frac{\sum_{i=1}^{N_\sigma}\left(\left|\sigma^i_{meas}{}^*\right| - \left|\sigma^i_{mod}{}^*\right|\right)^2}{\sum_{i=1}^{N_\sigma}\left(\left|\sigma^i_{meas}{}^*\right| - \left\langle\left|\boldsymbol{\sigma}_{meas}{}^*\right|\right\rangle\right)^2} + \frac{\sum_{i=1}^{N_\sigma}\left(\theta^i_{meas} - \theta^i_{mod}\right)^2}{\sum_{i=1}^{N_\sigma}\left(\theta^i_{meas} - \langle\boldsymbol{\theta}_{meas}\rangle\right)^2}, \quad (1)$$

where R^2 is the coefficient of determination, N_σ is the number of conductivity

measurements at different frequencies (for a given mud at a given pore water salinity), $\left|\sigma^i_{meas}*\right|$ and $\left|\sigma^i_{mod}*\right|$ are the i^{th} measured and modelled complex conductivity magnitude, respectively, and $\langle\left|\boldsymbol{\sigma}_{meas}*\right|\rangle$ is the arithmetic mean of the measured complex conductivity magnitudes. In Eq. 1, θ^i_{meas} and θ^i_{mod} are the i^{th} measured and modelled minus phase-shift, respectively, and $\langle\boldsymbol{\theta}_{meas}\rangle$ is the arithmetic mean of the measured minus phase-shifts between injected current and measured voltage and defined for the complex conductivity as

$$\sigma^* = \sigma' + i\sigma'' = \left|\sigma^*\right|\exp(i\theta). \quad (2)$$

Table 3. Symbols, definitions and units of the output (deduced from the model) parameters.

Symbol	Definition	Unit
d_k (1)	Aggregate effective diameter	m
C^b_{NaCl}	NaCl concentration in bulk water	mol L^{-1}
ϕ_a	Aggregate porosity	dimensionless
ϕ	Mud porosity	dimensionless
Θ^d_w	Water volume fraction of the diffuse layer	dimensionless
Ξ_{in} (2)	Volume of the interlayer space over the diffuse layer and interlayer space volumes	dimensionless
σ_s*	Surface conductivity of the aggregates	S m^{-1}
σ_w	Water conductivity ($<\left\|\boldsymbol{\sigma}_w*\right\|>$)	S m^{-1}
σ^b_w	Bulk water conductivity	S m^{-1}
σ^d_w (3)	Diffuse layer water conductivity	S m^{-1}
φ_d	Electrical potential at the start of the diffuse layer	mV
$B^d_{\text{Na}^+}$	Average sodium ion mobility in the diffuse layer	m^2 s^{-1} V^{-1}
Q_V	Aggregate excess of charge per unit pore volume	C m^{-3}

(1) Parameter value computed from adjusted β_S value and inverted τ_k value.
(2) For montmorillonite only.
(3) Thick diffuse layer assumption (see related discussion in section 3 of Leroy *et al.* 2024).

The output parameters of the SIP model are reported in Table 3. Four output parameters are of particular importance to compare the model predictions to the petrophysical measurements

and to the parameters of petrophysical models developed at larger scale than the EDL scale (e.g., Weller *et al.* 2013). These parameters are mud clay porosity (ϕ) and cementation exponent of the clay aggregates (m) given access to the electrical formation factor (F) according to first Archie's law, water conductivity (σ_w) and clay surface conductivity (σ_s*). In addition, the average effective ion mobility of Na^+ cation in the diffuse layer ($B^d_{Na^+}$) is shown in Table 3 because Na^+ is the major ionic component influencing diffuse layer conductivity here. The $B^d_{Na^+}$ quantity (Leroy *et al.* 2024) was computed from

$$B^d_{Na^+} = \beta^d_{Na^+} + \frac{1}{\chi_d}\int_{x=0}^{x=\chi_d} \beta^d_{eo}(x)dx, \quad (3)$$

where $\beta^d_{Na^+}$ is the Na^+ ion mobility due to electromigration (considered to be equal to the related ion mobility in bulk water, i.e. $\beta^d_{Na^+} = \beta^b_{Na^+}$), χ_d is the diffuse layer thickness, x is the distance from the beginning of the diffuse layer and normal to the mineral wall, and β^d_{eo} is the electroosmotic contribution to surface conductivity. According to Leroy *et al.* (2015) $\chi_d = 2\chi_D$ where χ_D is the Debye length that is inversely proportional to bulk water ionic strength ($\chi_D = \kappa^{-1}$, see Eq. 25). The quantities $\beta^d_{Na^+}$ and $\beta^d_{eo}(x)$ were computed considering their dependence on bulk water salinity, temperature and of the electrical potential in the diffuse layer for $\beta^d_{eo}(x)$ (see Section 2.2.1).

We consider that the interlayer space of our montmorillonite samples, i.e., Na-Mt containing hydrated Na^+ cations, can occupy a significant part of the volume of the mud. Mud porosity and the relative part of the volume of the interlayer space of Na-Mt over the interlayer space and diffuse layer volume were computed using

$$\phi = \frac{V_{in} + V_w^d + V_w^b}{V_t}, \tag{4}$$

$$\Xi_{in} = \frac{V_{in}}{V_{in} + V_w^d}, \tag{5}$$

where, in the numerator of Eq. 4, the Stern layer volume, V_S, was considered equal to 0 m^3 (because the Stern layer can be considered part of the solid and of the small Stern layer thickness, $d_S \cong 0.5$ nm (Leroy *et al.* 2024), and to decrease the number of model parameters), V_{in} is the computed interlayer space volume (we took an interlayer space thickness $t_{in} = 1$ nm for Na-Mt) and V_w^d is the computed diffuse layer volume. Concerning t_{in}, according to the review paper of Tournassat *et al.* (2015), the thickness of a TOT layer is around 9.5 Å and the basal spacing at d_{001} is equal to about 20.5 Å for the four-layer hydrate state. Therefore, the corresponding thickness of the interlayer space, t_{in}, is equal to $20.5 - 9.5 = 11 \cong 10$ Å (1 nm).

2.2 Model

2.2.1 Electrochemical properties

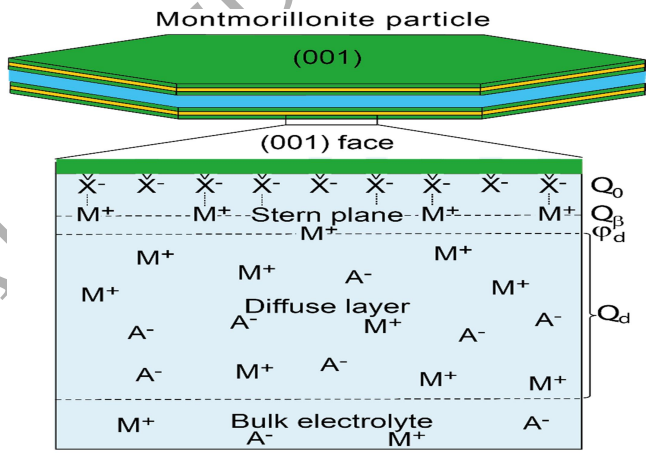

Figure 3. Sketch showing the electrochemical properties of the basal surface of montmorillonite in the case of a surrounding fully dissociated monovalent electrolyte like

NaCl. The quantities Q_β and Q_d are the surface charge densities of the Stern plane and of the diffuse layer, respectively.

The electrical potential at the beginning of the diffuse layer (from the mineral surface) (φ_d) (Fig. 3, for more details, see Fig. 5 of Leroy *et al.* 2024) is calculated from the measured temperature (T) (in K), bulk water salinity (C_b), mineral surface charge density (Q_0) and partition coefficient f_Q values. First the bulk water salinity (C_b) (in mol L^{-1}, M) was computed from the initial NaCl concentration (C^0_{NaCl}) and the measured sample masses before and after evaporation (δ_t^0 and δ_t^1, respectively). It was given by:

$$C_b = C^0_{\mathrm{NaCl}} \frac{\delta_t^0}{\delta_t^1}, \tag{6}$$

where $C_b = C^b_{\mathrm{NaCl}}$. The electrolyte was assumed fully dissociated implying

$$C_b = C^b_{\mathrm{Na^+}}, \tag{7}$$

and

$$C_b = C^b_{\mathrm{Cl^-}}. \tag{8}$$

The complex conductivity model depends on the specific surface area of the main clay mineral where cation exchange reactions occur (*SS*) (in meq g^{-1}) (Leroy *et al.* 2024). Among the *SS* values reported in Mendieta *et al.* (2021) (see supplementary material), only the specific surface area of illite measured by the BET (Brunauer-Emmett-Teller) method was considered for the complex conductivity modelling because the BET method cannot measure the internal specific surface area of smectite (Metz *et al.* 2005) and only the illite sample does not contain a significant smectite content according to X-ray diffraction (XRD) measurements (see Table 1 of Mendieta *et al.* 2021). The BET method probes the outer specific surface area

of clays by measuring adsorption isotherm of non-polar gases such as nitrogen or argon at low pressure and boiling temperature (77 K) (Tournassat *et al.* 2003). The specific surface area of the mineralogically heterogeneous kaolinite sample (containing significant smectite and illite contents, 4 % and 3 %, respectively) was adjusted by matching simulated to measured SIP spectra and the specific surface area of the green and red montmorillonite samples, which can be approximated by the total specific surface area of the basal surfaces (SS_b), was taken from crystallography (Table 4).

Table 4. Input microstructural, electrochemical, and mineralogical parameters

Clay samples	Kaolinite	Illite	Green Mt	Red Mt
SS (m^2 g^{-1})	29.78[(1)]	101.6[(2)]	760[(3)]	760[(3)]
CEC (meq g^{-1})	0.10[(4)]	0.20[(4)]	1.32[(2)]	1.35[(2)]
ξ_c (%)	0.91[(2)]	0.67[(2)]	0.90[(2)]	0.66[(2)]
Q_0 (C m^{-2})[(5)]	-0.324	-0.190	-0.168	-0.171

(1) Adjusted by matching simulated to measured SIP spectra.
(2) Measured (from *Mendieta et al.* (2021)); note that for kaolinite, we took into account smectite and illite contents.
(3) *Leroy et al.* (2015) (crystallography).
(4) Computed according to XRD measurements and theoretical CEC values.
(5) Computed according to the CEC and the specific surface area (Eq. 9).

The Q_0 quantity was calculated from the CEC and associated specific surface area (*SS*) (Zhou & Gunter 1992) using

$$Q_0 = \frac{-eN_A \,\mathrm{CEC}}{10^3 SS}, \tag{9}$$

where e is the electron (or elementary) charge (~1.602×10^{-19} C) and N_A is the Avogadro number (~6.022×10^{23} mol^{-1}). The CEC values reported in Mendieta *et al.* (2021) for kaolinite and illite samples (0.22 and 0.47 meq g^{-1}, respectively) were too high to obtain realistic surface charge density measurements (see supplementary material). We thought that the CEC measurements reported in Mendieta *et al.* (2021) overestimate the CEC of kaolinite and in a lesser extent of illite samples – possibly because only the fraction of clay particles with size

below 1 micrometre was considered for the CEC measurements. Indeed, the CEC increases when the size of the investigated particles decreases (Shim *et al.* 2003). As a consequence, for kaolinite and illite samples, we ran our SIP model with theoretical CEC values using

$$\mathrm{CEC} = \sum_{i=1}^{N_c} w_i \, \mathrm{CEC}_i \,, \tag{10}$$

where N_c is the number of the different clay minerals, w_i is the solid content of clay mineral i given by XRD measurements and CEC_i is its CEC. In Eq. 10, we used a CEC value of 0.05 meq g^{-1} for kaolinite, 0.25 meq g^{-1} for illite, and 1 meq g^{-1} for smectite (Revil & Leroy 2004, and Table 4). With the theoretical CEC values for kaolinite and illite samples and the measured CEC values of montmorillonites, we obtained $Q_0 = -0.324$ C m^{-2} for kaolinite, $Q_0 = -0.190$ C m^{-2} for illite, $Q_0 = -0.168$ C m^{-2} for green montmorillonite, and $Q_0 = -0.171$ C m^{-2} for red montmorillonite samples (Table 4 and Eq. 9). Using these values divided by the electron charge, we estimated that kaolinite, illite, green and red montmorillonite samples have ~2.014, 1.186, 1.046, and 1.067 elementary charges nm^{-2} on their surface, respectively, which is in the range of the 1 to 3 elementary charges nm^{-2} expected for clay minerals (Revil & Leroy, 2004; see their Figure 2).

The electrical potential at the beginning of the diffuse layer φ_d is required to compute (i) the electrical conductivity of the diffuse layer, (ii) the conductivity of the part of the interlayer space of Na-Mt not contributing to polarisation (see Leroy *et al.* 2024), and (iii) the effect of the diffuse layer on Stern layer polarisation according to Lyklema *et al.* (1983). These latter authors assumed that the counter-ions in the diffuse layer decrease the relaxation time associated with the polarised Stern layer. In our model, this effect can be modelled through the computation of the *M* parameter (see Leroy *et al.* 2024). The φ_d potential is calculated

from the measured temperature T (in K, $T = T_C + 273.15$), C_b, Q_0 and f_Q values by solving

$$\left| \sqrt{4\overline{\varepsilon_w} k_B T 1000 N_A C_b \left[\cosh\left(\frac{e\varphi_d}{k_B T} \right) - 1 \right]} - Q_0 \left(1 - f_Q \right) \right| = 0 , \quad (11)$$

where $\overline{\varepsilon_w}$ represents the average water permittivity in the diffuse layer (on clay particle surface) and interlayer space (in the clay particle) of Na-Mt (in F m^{-1}), and k_B is the Boltzmann's constant (~1.381×10^{-23} J K^{-1}).

It should be noted that the water permittivity term ($\overline{\varepsilon_w}$) intervening in Eq. 11 is assumed to be related to the bulk water permittivity (ε_w) and to the permittivity of the interlayer space of Na-Mt that is assumed to be half the bulk water permittivity (see discussion in Tournassat *et al.* 2009 and in section 3.2 of Leroy *et al.* 2024). We assume that the water permittivity of the diffuse layer around clay particles is equal to bulk water permittivity. The term $\overline{\varepsilon_w}$ is calculated from the water permittivities in the diffuse layer and interlayer space weighted by their respective relative volume fraction, i.e.

$$\overline{\varepsilon_w} = \frac{\varepsilon_w}{V_w^d + V_{in}} \left(V_w^d + \frac{V_{in}}{2} \right) , \quad (12)$$

where ε_w depends on temperature (in the temperature range 2-87°C, for more related information read Leroy *et al.* 2024). In Eq. 12, the V_w^d and V_{in} quantities were determined from

$$V_w^d = 2\delta_s \xi_c SS_0 \chi_D , \quad (13)$$

where SS_0 is the outer specific surface area of clay particles (in m^2 g^{-1}) and $\chi_D = \kappa^{-1}$ is the

Debye length (in m), and

$$V_{in} = \frac{\delta_s \xi_c SS}{2n_c}\left(n_c - 1\right)t_{in}\,. \tag{14}$$

We considered in Eq. 13 from Leroy *et al.* (2024) that the outer specific surface areas of the clay particles in kaolinite and illite samples are equal to SS (i.e. $SS_o = SS$) and that the outer specific surface areas of the clay particles in montmorillonite samples are equal to SS / n_c (i.e. $SS_o = SS / n_c$). In the case of montmorillonite, we assumed in Eq. 14 from Leroy *et al.* (2024) that $SS = SS_b$ with SS_b being the total specific surface area of the basal surfaces (see Appendix A of Leroy *et al.* 2024, for details).

2.2.2 Surface conductivity and effective size distribution of the aggregates

The SIP model considers that the clay mud is composed of the solid part of the clay aggregates (including Stern layers on particle surfaces) and of Na-Mt interlayer spaces, bulk and diffuse layer waters (case of the thick diffuse layer assumption in the model of Leroy *et al.* 2024), and weakly conductive and polarisable minerals (Fig. 1). Because Na-Mt particles contain hydrated and mobile Na^+ cations in their interlayer space (Bourg *et al.* 2003), we assumed that the interlayer space of Na-Mt behaves like an EDL containing a Stern and a diffuse layer. In our model, the excess of charge per unit pore volume of the clay aggregate (Q_V) (in C m^{-3}) is the main parameter controlling electrochemical polarisation, like in the model of Vinegar & Waxman (1984). The Q_V quantity was computed according to the solid volumetric mass density (ρ_s) (in kg m^{-3}), computed porosity of the clay aggregate (ϕ_a), and measured CEC using

$$Q_V = \rho_s \left(\frac{1-\phi_a}{\phi_a} \right) e N_A \, \mathrm{CEC}, \tag{15}$$

where ϕ_a depends on the calculated volumes of the different components of the aggregate

$$\phi_a = \frac{V_w^d + V_w^b}{V_{sc} + V_w^d + V_w^b}, \tag{16}$$

for kaolinite, and

$$\phi_a = \frac{V_w^d}{V_{sc} + V_w^d}, \tag{17}$$

for illite, and

$$\phi_a = \frac{V_{in} + V_w^d}{V_{sc} + V_{in} + V_w^d}, \tag{18}$$

for montmorillonite such as Na-Mt, where V_{sc} and V_w^b are the computed volumes of the solid clay layers (in m^3) and bulk water, respectively (for more details, see Appendix A of Leroy *et al.* 2024)

$$V_s = \frac{10^{-3} \delta_s}{\rho_s}, \tag{19}$$

$$V_{sc} = V_s \xi_c, \tag{20}$$

$$V_w^b = 10^{-6} V_t - V_s - V_w^d - V_{in}, \tag{21}$$

where we took $\rho_s = 2700$ kg m^{-3} for the solid volumetric mass density (Tournassat *et al.* 2016) and we neglected illite interlayer space and Stern layer volumes in the calculation of the aggregate porosity to decrease the number of model parameters. It should be noted that we

assumed in Eqs 17 and 18 that illite and montmorillonite aggregates contain only diffuse layer (and interlayer space for Na-Mt) in their pores. Therefore, in these conditions, computed aggregate porosity ϕ_a is not necessarily identical to computed mud porosity ϕ because mud can also contain bulk water (see Eq. 4). In Leroy *et al.* (2024), we considered that a pure kaolinite aggregate also contains bulk water, but, in the SIP experiment of Mendieta *et al.* (2021), kaolinite sample contains significant illite and smectite solid contents (3 % and 4 %, respectively) that may explain why we had to consider only diffuse layer water in the clay aggregates of the kaolinite sample ($V_w^b = 0\ \mathrm{m}^3$ in Eq. 16).

The surface conductivity of the clay aggregate due to Stern layer polarisation (σ_s^*; in S m^{-1}), was determined as a function of the angular frequency ω (in rad s^{-1}) using

$$\sigma_s^*(\omega) = \frac{2}{3}\phi_a \beta_S f_Q Q_V \sum_{k=1}^{L} f(d_k) \frac{i\omega\tau_k}{1+i\omega\tau_k} + i\omega\alpha\rho_s\varepsilon_0, \quad (22)$$

where $f(d_k)$ is the aggregate size distribution, with $k = 1 \ldots L$ (L being the number of different aggregate effective diameters and d_k being the effective diameter of the k^{th} aggregate), i is the imaginary number ($i^2 = -1$) and τ_k is the relaxation time of the polarised Stern layers around interacting clay particles within the k^{th} aggregate (in s) (Leroy *et al.* 2024). In Eq. 22, $\alpha = 0.00191$ m^3 kg^{-1} is an empirical value that was used by Olhoeft (1981) to adjust solid dielectric permittivity spectra in absence of conducting materials, such as magnetic or metallic minerals, and Fe Ti sulphides oxides such as ilmenite, $\varepsilon_0 \cong 8.854\times10^{-12}$ F m^{-1} is the permittivity of vacuum, and $\kappa = \chi_{\mathrm{D}}^{-1}$ is the inverse of the Debye length (in m^{-1}).

According to Leroy *et al.* 2024, aggregate effective size distribution was computed from

$$d_k = \sqrt{8\frac{k_B T}{e}\beta_S M \tau_k}\,, \tag{23}$$

$$M = 1 - \frac{f_Q Q_0}{k_B T \overline{\varepsilon_w} \kappa \cosh\left(\frac{e\varphi_d}{2k_B T}\right)}, \tag{24}$$

$$\kappa = \sqrt{\frac{2e^2 10^3 N_A C_b}{\overline{\varepsilon_w} k_B T}}\,. \tag{25}$$

2.2.3 Water conductivity

Our model calculates water conductivity (σ_w^*) from the computed bulk water conductivity (σ_w^{b*}) and diffuse layer water (and Na-Mt interlayer space) conductivity (σ_w^{d*}) using the lower bound of the self-consistent model developed by Hashin & Shtrikman (1962):

$$\sigma_w^* = \sigma_w^{b*}\left[1 + \frac{3\Theta_w^d\left(\sigma_w^{d*} - \sigma_w^{b*}\right)}{3\sigma_w^{b*} + \left(1-\Theta_w^d\right)\left(\sigma_w^{d*} - \sigma_w^{b*}\right)}\right], \tag{26}$$

where Θ_w^d is the volume fraction of diffuse layer water over diffuse layer and bulk waters. In Eq. 26, the condition $\left|\sigma_w^{d*}\right| > \left|\sigma_w^{b*}\right|$ that is usually considered on particle surface (explaining surface conductivity (Revil & Glover 1997; Lyklema & Minor 1998)) should be satisfied.

Bulk water and diffuse layer conductivities were calculated from

$$\sigma_w^{b*} = e10^3 N_A\left(\beta_{Na^+}^b + \beta_{Cl^-}^b\right)C_b + i\omega\varepsilon_w\,, \tag{27}$$

$$\sigma_w^{d*} = \frac{e10^3 N_A C_b}{\chi_d}\int_{x=0}^{x=\chi_d}\left\{B_{Na^+}^d(x)\exp\left[-\frac{e\varphi(x)}{k_B T}\right] + B_{Cl^-}^d(x)\exp\left[\frac{e\varphi(x)}{k_B T}\right]\right\}dx + i\omega\overline{\varepsilon_w}\,, \tag{28}$$

$$B^d_{Na^+}(x) = \beta^b_{Na^+} + \beta^d_{eo}(x), \tag{29}$$

$$B^d_{Cl^-}(x) = \beta^b_{Cl^-} - \beta^d_{eo}(x), \tag{30}$$

$$\beta^d_{eo}(x) = \frac{\varepsilon_w}{\eta_w}\left[\varphi(x) - \varphi_d\right], \tag{31}$$

where $\beta^b_{Na^+}$ and $\beta^b_{Cl^-}$ are the Na^+ and Cl^- ion mobilities (in $m^2\ s^{-1}\ V^{-1}$) due to ion electromigration under the applied electrical field that were corrected of temperature using water dynamic viscosity measurements, η_w (in Pa s^{-1}), and salinity (see Appendix B of Leroy *et al.* 2024). In Eq. 28, $B^d_{Na^+}$ and $B^d_{Cl^-}$ are the effective ion mobilities of Na^+ and Cl^- ions in the diffuse layer considering electroosmosis and φ is the electrical potential in the diffuse layer (in V). The electrical potential φ was computed by solving analytically the Poisson-Boltzmann equation (see Section 3.4 of Leroy *et al.* 2024):

$$\varphi(x) = \frac{4k_B T}{e}\tanh^{-1}\left[\tanh\left(\frac{e\varphi_d}{4k_B T}\right)\exp\left(-\kappa x\right)\right]. \tag{32}$$

Because we used the diffuse layer electrical conductivity model based on the φ_d potential calculation, we did not use here the diffuse layer electrical conductivity model based on the calculation of the average electrical potential in the diffuse layer (φ_m), which is reported in Okay *et al.* (2014) and in Leroy *et al.* (2024). Indeed, we assume here that the Poisson-Boltzmann equation is more accurate to estimate the electrical potential distribution in the diffuse layer than using directly an average electrical potential. In addition, the calculation of the φ_d potential allows directly computing the effect of the diffuse layer on Stern layer polarisation represented in the model by the *M* parameter (Eq. 24).

2.2.4 Mud clay complex conductivity

In our model, the background conductivity of clay mud (not considering surface conductivity effect) (σ_0^*) is corrected of the effect of minerals less conductive than water using the upper bound of the self-consistent model developed by Hashin & Shtrikman (1962):

$$\sigma_0^* = \sigma_w^* \left[1 - \frac{3(1-c)}{(3-c)} \right], \tag{33}$$

where c is the volume fraction of conductive water over the volume of considered not conductive minerals and conductive water. The effect of magnetite, which is a metallic mineral that may be more conductive than clays, was neglected in our model because of its small content (1 %) in red montmorillonite sample (Mendieta *et al.* 2021).

After computing σ_0^*, the self-consistent assumption of the differential effective medium theory (Bruggeman-Hanai-Sen (BHS) model; Mendelson & Cohen 1982; Sen 1984) was used to calculate clay mud complex conductivity (σ^*) considering inclusions of randomly oriented solid clay aggregates of cementation exponent m with volume fraction $d\Omega_s$ and surface conductivity σ_s^* in the background medium up to reach the solid clay content in the sample ($\Omega_s = 10^6 V_{sc} / V_t$):

$$L = \frac{3 + \sqrt{9 + 36m^2 - 60m}}{6m}, \tag{34}$$

$$d\sigma^* = \frac{\sigma^*}{3} \frac{(\sigma_s^* - \sigma_0^*)\left[(1+3L)\sigma_s^* + (5-3L)\sigma_0^*\right]}{\left[L\sigma_s^* + (1-L)\sigma_0^*\right]\left[(1-L)\sigma_s^* + (1+L)\sigma_0^*\right]} \frac{d\Omega_s}{1-\Omega_s}, \tag{35}$$

$$\sigma^* = \sigma^* + d\sigma^*, \tag{36}$$

$$\Omega_s = \Omega_s + d\Omega_s , \tag{37}$$

where L is the depolarisation factor of inclusions ($0 \le L \le 1$), $\Omega_s = 0$ and $\sigma^* = \sigma_0{}^*$ initially and $d\Omega_s = 10^6 V_{sc} / \left(V_t N_s\right)$ with N_s being the number of randomly oriented solid inclusions. The procedure outlined in Eqs 34-37 is sensitive to the value of the cementation exponent *m* and allows also simulating Maxwell-Wagner polarisation (Leroy & Revil 2009).

Aggregate eccentricity (e_c) was also deduced from the depolarisation factor L calculation (Mendelson & Cohen 1982) based on optimised cementation exponent *m* value (Eq. 34) by solving

$$\left| L - \frac{1+e_c{}^2}{e_c{}^3}\left(e_c - \tan^{-1} e_c\right) \right| = 0 , \tag{38}$$

and then, according to Mendelson & Cohen (1982), the height of the k^{th} aggregate (in m) with effective diameter d_k was given by

$$h_k = \sqrt{\frac{d_k{}^2}{1+e_c{}^2}} . \tag{39}$$

2.3 Optimisation procedure

First of all, it should be noted that the measured conductivity $\sigma_{meas}{}^*(\omega)$ is not equal to $\sigma_{mod}{}^*(\omega)$ ($\sigma_{mod}{}^*(\omega)$ being the prediction of the model developed in Leroy *et al.* (2024)) but it is equal to $\sigma_{mod}{}^*(\omega) + i\omega C_c$. The $i\omega C_c$ term is introduced here to take into account the contact impedance of the potential electrodes and electromagnetic coupling effects between cables during the measurements (Ingeman-Nielsen & Baumgartner 2006; Florsch *et al.* 2014;

Huisman *et al.* 2016). It should be also noticed that the C_c values determined during the optimization procedure (see Appendix B) are different from the *C* values obtained during the Debye decomposition procedure (see Appendix A). Indeed, in the model developed in Leroy *et al.* (2024), the displacement current is taken into account. The C_c values obtained here are therefore the effects of the contact impedance of the potential electrodes and electromagnetic coupling only. The corrected spectra are the spectra from which the $i\omega C_c$ curve has been subtracted.

For each clay type, we used a simulated annealing algorithm (see Maineult 2016) and then the simplex algorithm to determine the best values of the model parameters using the spectra at 0.01 M NaCl initially and 0.10 M NaCl initially together. For kaolinite, the "common" parameter was *SS*, the "individual" parameters were f_Q, mr_S, and *m*, and the coupling coefficient C_c (here, "common" means that the value is not dependent on salinity, and "individual" means that there is a value of the parameter per salinity, see Tables 4 and 5). For illite, all the parameters, i.e., f_Q, mr_S, *m*, and C_c were individual. For montmorillonite, the common parameter was mr_S, the individual ones were f_Q, *m*, and C_c, and the values of n_c were determined by a systematic exploration. Note that red montmorillonite at 1 M NaCl initially was optimised separately. We assumed a constant value of mr_S in the case of montmorillonite for the two lowest salinities because of the stronger influence of the isomorphic substitutions in the solid crystal compared to kaolinite and illite, inducing a constant negative attractive force slowing down cations with the same strength in the Stern layer.

3 COMPARISON TO EXPERIMENTAL DATA AND DISCUSSION

3.1 SIP data representation and model parameter optimisation

The complex conductivity magnitude and minus phase-shift can be expressed as a function of the real part of the complex conductivity (in-phase conductivity) and the imaginary part of the complex conductivity (quadrature conductivity) using:

$$|\sigma^*| = \sqrt{\sigma'^2 + \sigma''^2}\,, \tag{40}$$

$$\theta = \tan^{-1}\left(\frac{\sigma''}{\sigma'}\right), \tag{41}$$

It is easier to understand in-phase and quadrature conductivities rather than magnitude and minus phase-shift of the complex conductivity because σ' is mostly sensitive to conduction current and σ'' is only sensitive to polarisation current (Okay *et al.*, 2014), whereas $|\sigma^*|$ and θ are a combination of both σ' and σ''. In addition, because $|\sigma'| >> |\sigma''|$, $|\sigma^*| \cong |\sigma'|$ (Eq. 40). Therefore, in the following, we only discussed complex conductivity magnitude or in-phase conductivity, and not complex conductivity magnitude and in-phase conductivity (see Fig. 4 for instance). Nevertheless, we present $|\sigma^*|$, θ, and σ', σ'' because complex conductivity measurements are usually represented in terms of $|\sigma^*|$ and θ. The magnitude and minus phase-shift of the complex conductivity as well as the in-phase conductivity and the quadrature conductivity and the aggregate effective size distribution of each clay sample are reported in Figs 4 to 8. The results of the optimisation procedure are shown in Tables 5 and 6 (optimised parameter values are given with four digits after coma to enable people to reproduce the results).

The parameter values were well constrained (uncertainties below 10 % of the main value) (see

supplementary material). Varying infinitesimally these parameter values from their optimised values induces a more than 50 % increase of the cost function (Eq. 1) (except for the case of the number of platelets per particle (n_c) for red montmorillonite at 1 M NaCl initially).

The effective ion mobility of Na^+ counter-ion in the Stern layer of the main clay mineral was computed from mr_S and the temperature T (K) (Revil *et al.* 1998), with:

$$\beta_S = mr_S \overline{\beta}^b_{Na^+}(298)\left[1 + v_S\left(T - 298.15\right)\right], \tag{42}$$

where $\overline{\beta}^b_{Na^+}(298) \cong 5.19\times10^{-8}$ m^2 s^{-1} V^{-1} and $v_S = 0.037$ K^{-1} (Leroy *et al.* 2024).

Mineral surface charge influences surface ion mobility of counter-ions in the Stern layer and interlayer space by slowing down counter-ion species and water molecules (Bourg & Sposito 2011; Greathouse *et al.* 2016; Bouhadja & Skelton 2018). In our model, the magnitude of the surface charge density of the main clay mineral (Q_0) is fixed and linearly proportional to the CEC (Eq. 9). In the case of pure kaolinite, the surface ion mobility of counter-ions in the Stern layer can decrease with increasing salinity because of the stronger surface charge density attracting and slowing down more strongly counter-ions in the Stern layer (Bouhadja & Skelton 2018). Indeed, when salinity increases, at constant pH, deprotonation of surface hydroxyl sites and the increasing concentration of counter-ions in the Stern layer increases the magnitude of the negative surface charge density of the mineral (Sahai & Sverjensky 1997). In the case of 0.01 and 0.1 M NaCl initially, the constant CEC of montmorillonite minerals when salinity changes (due to the permanent and negative structural surface charge) implies an electrostatic attraction force slowing down counter-ions with the same strength whatever salinity. However, at initial salinities of 0.1 M NaCl and 1 M NaCl, Na^+ effective ion mobility on the surface of illite and red montmorillonite, respectively, can decrease compared to those at lower initial salinities because of particle coagulation and the higher Na^+ concentration

combined with the more hydrophobic clay surface (Greathouse *et al.* 2016). In addition, our kaolinite sample contains a significant solid content of smectite (4 %) and illite (3 %), which may control the electrochemical properties of the sample due to the higher structural surface charges and considerably higher specific surface areas of montmorillonite (typically 700-800 $m^2\ g^{-1}$) and illite (typically 100-200 $m^2\ g^{-1}$) particles than kaolinite particle (typically 10-20 $m^2\ g^{-1}$) (Tournassat *et al.* 2003; Hassan *et al.* 2006; Tournassat *et al.* 2015) (see related discussion in Leroy *et al.* 2024). Therefore, we assumed that Na^+ effective ion mobility on clay particle surface in the kaolinite sample is not changing significantly with salinity (see Table 5).

3.2 Results and discussion

3.2.1 SIP and aggregate size distribution spectra

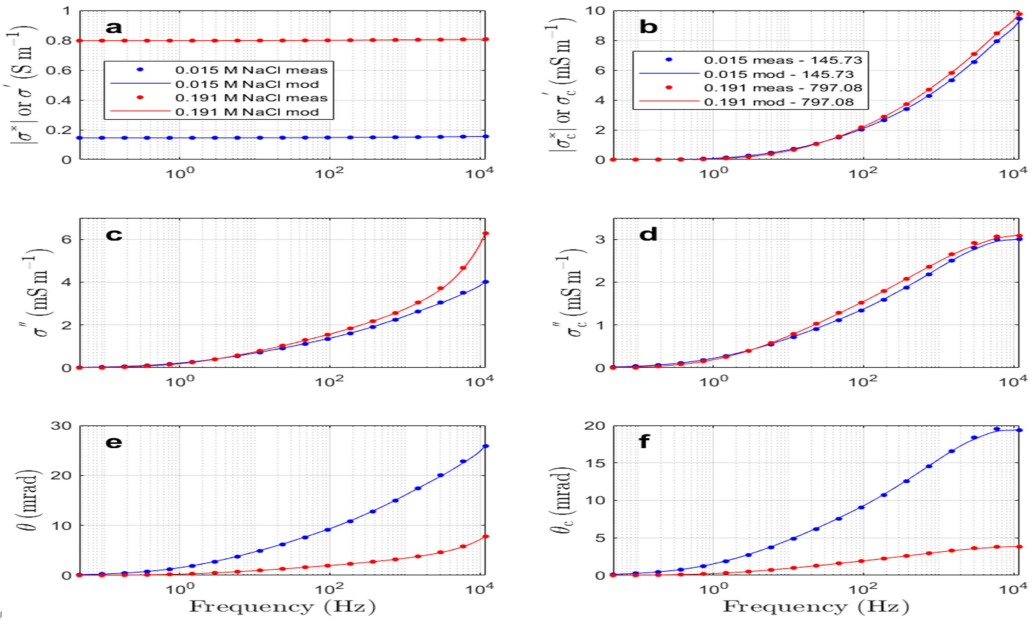

Figure 4. Complex conductivity of kaolinite muds at two NaCl concentrations ($C_b = 0.0154$ M and $C_b = 0.191$ M). Measurements (filled circles) and modelling results (curves). **a**: raw real part, **c**: raw imaginary part, **e**: raw phase, **b**, **d**, **f**: same as **a**, **c**, **e** but after removing the

coupling term (in **b**, the in-phase conductivity at the lowest frequency is also removed).

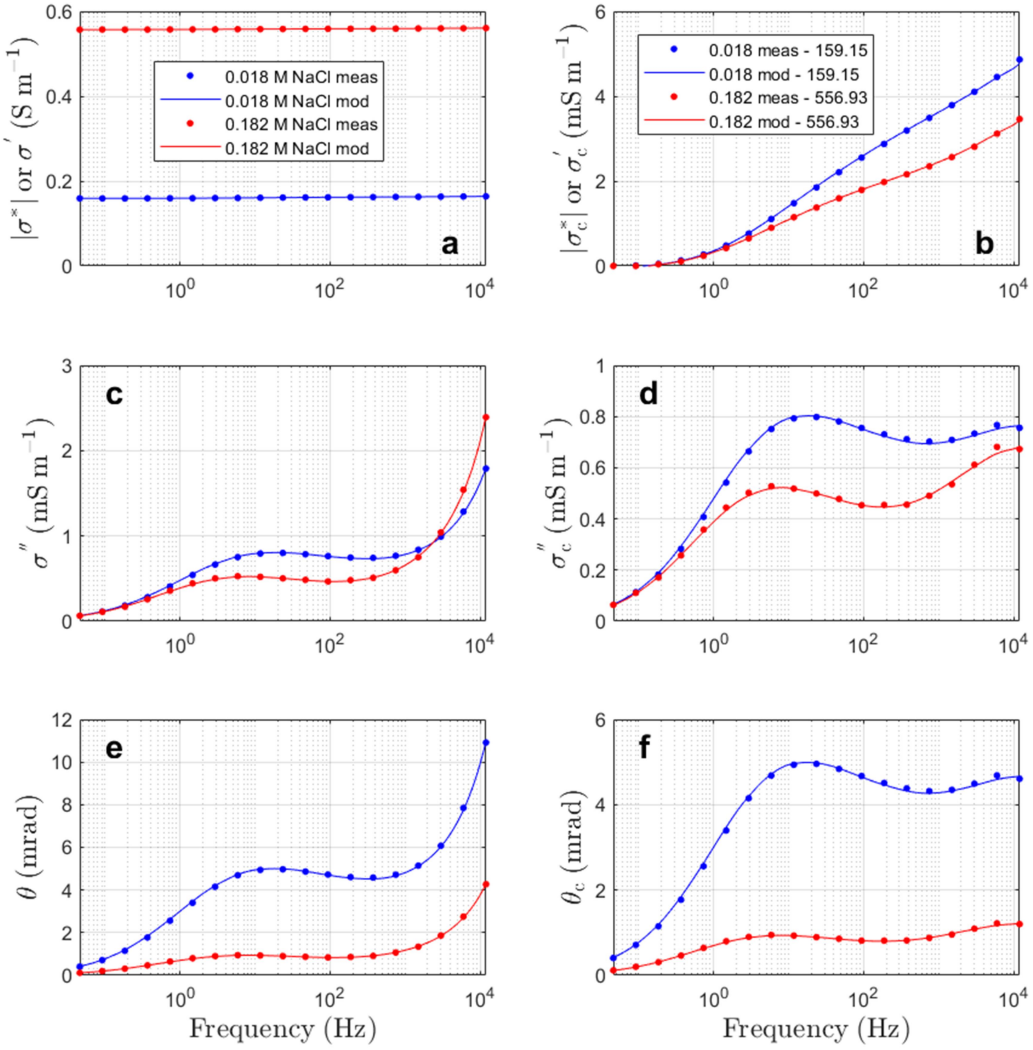

Figure 5. Complex conductivity of illite muds at two NaCl concentrations ($C_b = 0.0180$ M and $C_b = 0.182$ M). Measurements (filled circles) and modelling results (curves). **a**: raw real part, **c**: raw imaginary part, **e**: raw phase, **b**, **d**, **f**: same as **a**, **c**, **e** but after removing the coupling term (in **b**, the in-phase conductivity at the lowest frequency is also removed).

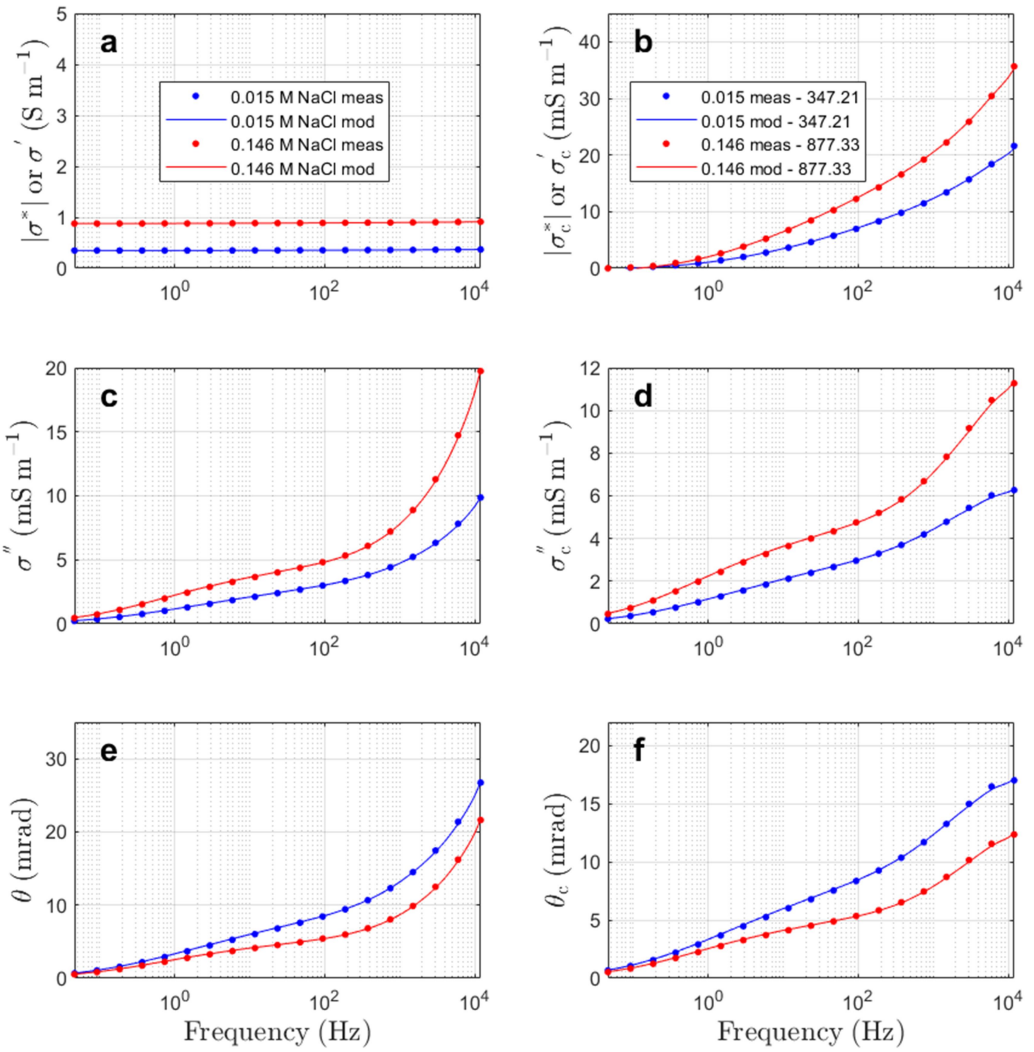

Figure 6. Complex conductivity of green montmorillonite muds at two NaCl concentrations ($C_b = 0.0153$ M and $C_b = 0.146$ M). Measurements (filled circles) and modelling results (curves). **a**: raw real part, **c**: raw imaginary part, **e**: raw phase, **b**, **d**, **f**: same as **a**, **c**, **e** but after removing the coupling term (in **b**, the in-phase conductivity at the lowest frequency is also removed).

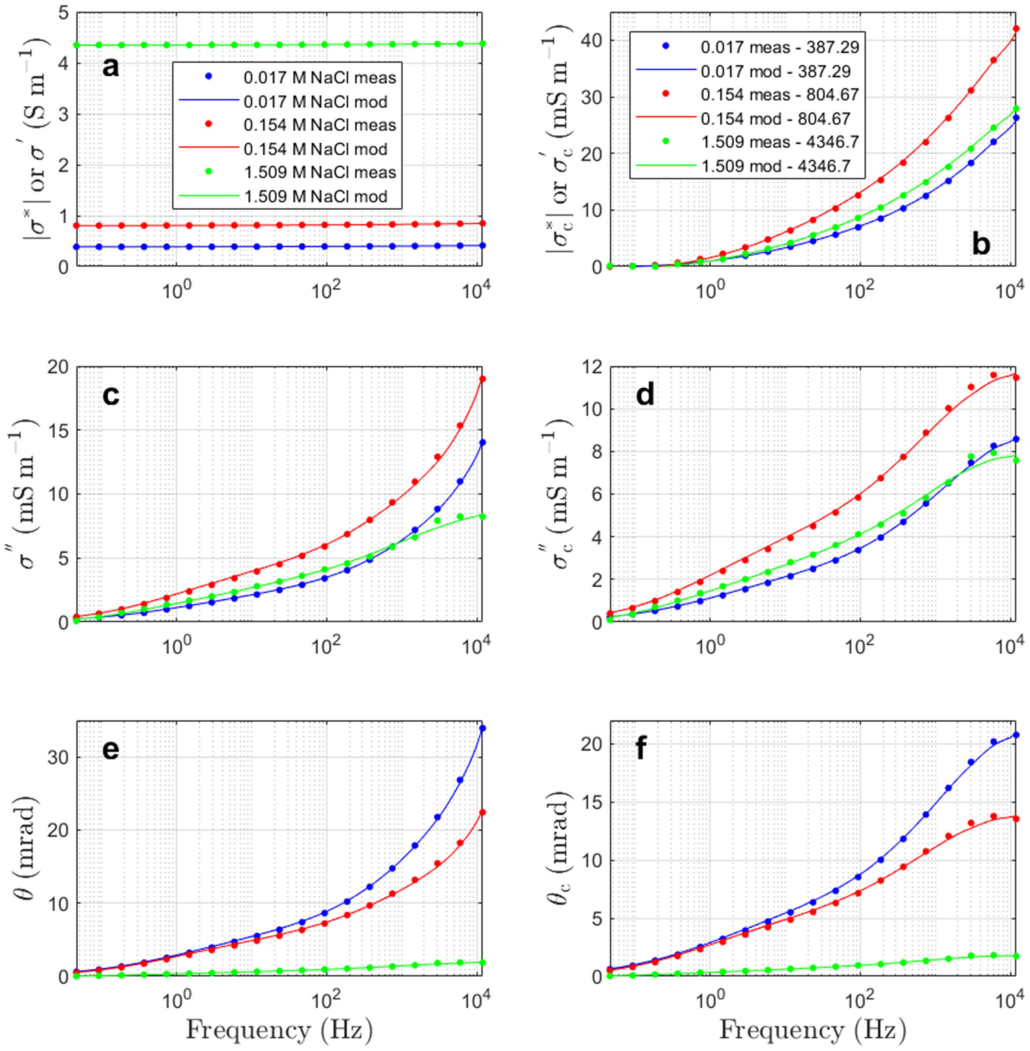

Figure 7. Complex conductivity of red montmorillonite muds at three NaCl concentrations ($C_b = 0.0171$ M, $C_b = 0.154$ M, and $C_b = 1.51$ M). Measurements (filled circles) and modelling results (curves). **a**: raw real part, **c**: raw imaginary part, **e**: raw phase, **b**, **d**, **f**: same as **a**, **c**, **e** but after removing the coupling term (in **b**, the in-phase conductivity at the lowest frequency is also removed).

After running the optimisation procedure, our model reproduces very well the experimental data (see Figs 4 to 7 and the cost-function values reported in Table 5). The model is able to reproduce the observed increase of in-phase conductivity σ' when salinity increases by considering increasing water conductivity σ_w (Table 6). We also showed in Table 6 the computed bulk conductivity values considering the presence of not conducting minerals $\sigma_0 = <|\boldsymbol{\sigma}_0^*|>$ (Eq. 33). Measured data corrected from coupling effects show more reliable

behaviour at high frequency. The measured increase of σ' when frequency increases, which can be clearly seen for frequencies above 0.1 Hz, was also reproduced in our model by simulating Stern layer polarisation. As shown earlier by Okay *et al.* (2014) and Leroy *et al.* (2017), the observed quadrature conductivity σ'' is less sensitive to salinity than the observed in-phase conductivity because of the structural charge influence on polarisation. Indeed, the permanent and negative structural charge adsorbs a large quantity of mobile cations in the Stern layer on the surface of clay particles, which controls electrochemical polarisation and then quadrature conductivity (σ''). Observed quadrature conductivity has a tendency to increase when salinity increases. We explain such observation by the increasing excess of charge per unit pore volume in the Stern layers within the aggregate contributing to polarisation, i.e., the product $f_Q Q_V$ (Tables 5 and 6). However, effective ion mobility of Na^+ counter-ion in the Stern layer on clay surface, β_S, also influences electrochemical polarisation. In our model, the decrease of β_S when salinity increases explains the observed decrease of the quadrature conductivity of illite at 0.1 M NaCl initially and of red montmorillonite at 1 M NaCl initially. The β_S values are also considerably smaller, i.e. about two orders of magnitude smaller, than the ion mobility value of Na^+ ion in bulk and distilled water, in agreement with Revil (2012). We think that these β_S values are effective Na^+ ion mobility values and do not correspond directly to the local Na^+ ion mobility value in the Stern layer. The latter can be inferred from molecular dynamic simulations. According to e.g. Tournassat *et al.* (2009) and Bourg & Sposito (2011), its value is considerably larger than our β_S values, and is about half Na^+ ion mobility value in bulk and distilled water. Leroy *et al.* (2017) were able to reproduce complex conductivity measurements on dispersed montmorillonite suspensions (less than one hundred grams of solid clay per litre of dispersion) using the same model as we, considering $\beta_S \cong 0.42\overline{\beta}^b_{Na^+}(298)$. As we were

dealing here with considerably more concentrated clay muds (around one thousand grams of solid clay per litre of mud, Table 1), our opinion is that the interaction between clay particles decreases Na^+ ion effective mobility in the Stern layer. Our computations also reproduce minus phase-shift measurements that depend on the ratio of σ" to σ'.

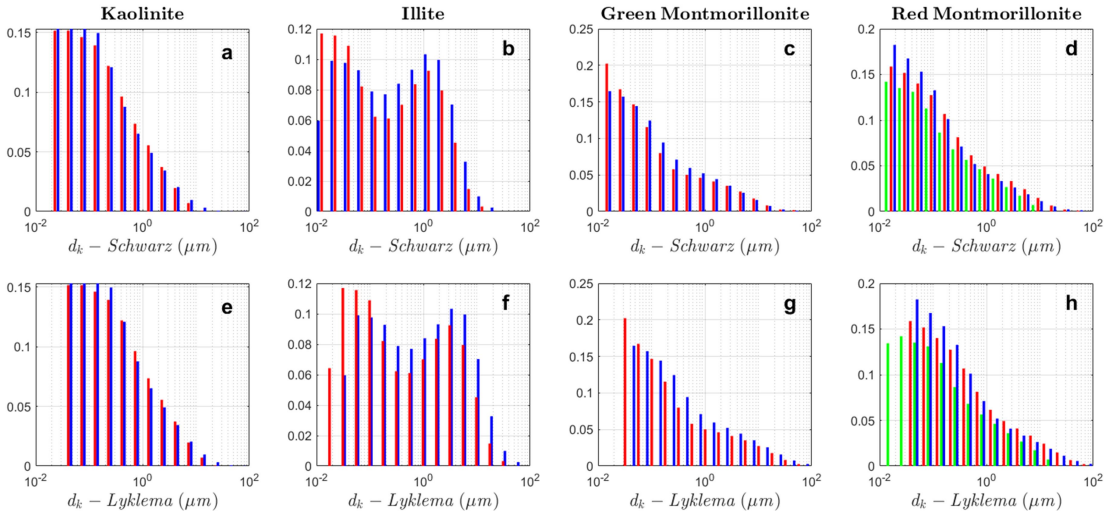

Figure 8. Aggregate effective size distributions inferred from the computation of the complex conductivity of clay muds at three initial NaCl concentrations (blue: 0.01 M NaCl, red: 0.1 M NaCl, green: 1 M NaCl initially; top: $M = 1$ according to the original model by Schwarz (1962); bottom: M computed by Lyklema *et al.* (1983) model).

Fig. 8 shows the aggregate size distributions inferred from the comparison of the model predictions to the corresponding experimental data. Aggregate size distributions are in the µm range expected for clay aggregates (Tombacz & Szekeres 2004, 2006; Jiang *et al.* 2022) and are relatively similar between each type of clay except for illite that shows two distinguishable peaks. It looks that the presence of a high smectite content in the kaolinite sample can explain similarity in observable aggregate size distributions between kaolinite and montmorillonite samples. In the illite sample, the presence of an additional peak for large sizes can be explained by the presence of large grains like calcite grains coated by illite particles (calcite solid content of 12 %, Mendieta *et al.* 2021). On the contrary to what has been observed in Leroy *et al.* 2017 for Na-Mt clay dispersions, aggregate size distributions do

not exhibit here large changes when salinity increases. In particular, we did not see here a peak corresponding to larger aggregates due to clay particle coagulation at the highest salinities. The clay muds investigated here are considerably more concentrated than the dispersed suspensions used in Leroy *et al.* 2017 (~1000 g versus ~10 g clay powder per sample litre). Due to the considerably higher clay content with interacting clay particles, the SIP data showed here are flatter in frequency with larger magnitudes and are less-changing with salinity especially in the low-frequency range (typically below 1 Hz) than the SIP data reported in Leroy *et al.* (2017). It would be interesting to validate or not our modelling results by aggregate size distribution measurements using high resolution characterisation techniques such as X-ray microtomography (Massat *et al.* 2016) and wide angle X-ray scattering (Chaaya *et al.* 2023).

3.2.2 Output model parameter values (optimised)

Table 5. Output model parameter values (optimised in bold) inferred from the computation of the complex conductivity of clay muds at different NaCl concentrations and corresponding cost function (y) values.

Clay	C_b (M)	f_Q	Q_β [(1)] (C m^{-2})	$10^2 mr_S$	$10^{10}\beta_S$ [(2)] (m^2 s^{-1} V^{-1})	n_c	m	$10^3 y$
Kaolinite	1.540×10^{-2}	**0.5135**	0.1664	**7.394**	33.63	1	**1.500**	0.43
	1.908×10^{-1}	**0.5347**	0.1732	**6.979**	26.12	1	**1.500**	0.22
Illite	1.804×10^{-2}	**0.8265**	0.1570	**1.268**	5.794	1	**1.697**	0.67
	1.816×10^{-1}	**0.8267**	0.1571	**0.722**	2.475	1	**1.697**	0.50
Green Mt	1.528×10^{-2}	**0.7900**	0.1327	**3.166**	13.61	**2**	**1.500**	0.60
	1.457×10^{-1}	**0.7213**	0.1212	**3.166**	10.59	**2**	**2.031**	0.43
Red Mt	1.708×10^{-2}	**0.7592**	0.1298	**3.796**	17.89	**2**	**1.500**	0.53
	1.541×10^{-1}	**0.7509**	0.1284	**3.796**	13.41	**2**	**1.922**	1.47
	1.509	**0.8388**	0.1434	**0.595**	2.720	**25**	**2.367**	4.78

(1) Using Q_0 values (Table 4) and optimised f_Q values and Eq. 43.

(2) Using optimised mr_S values and Eq. 42.

In our model, the fraction of the counter-charge in the Stern layer was defined as

$$f_Q = \frac{Q_\beta}{Q_\beta + Q_d} = -\frac{Q_\beta}{Q_0}, \tag{43}$$

where Q_β is the surface charge density of the Stern layer and Q_d is the surface charge density of the diffuse layer (Leroy *et al.* 2024). We consider here a constant CEC and a mineral surface charge density Q_0 for each type of clay sample (kaolinite, illite and montmorillonite). Therefore, f_Q changes induce associated Q_β changes and an increasing f_Q means an increasing surface charge density of the Stern layer. Because the permanent structural charge of the basal surfaces controls the EDL properties of the clays, the value of Q_β is high and relatively constant, as we can see in Table 5.

The Stern layer makes up more than 50 % of the counter-charge on the external clay particle surface, at least for the basal surfaces of illite and montmorillonite containing a high structural charge (Tournassat *et al.* 2009; Bourg & Sposito 2011; Tournassat *et al.* 2015; Tinnacher *et al.* 2016). We found that about 51 % to 84 % of the surface charge density of the EDL polarizes (f_Q values in Table 5), confirming that the Stern layer polarisation process may control the electrochemical polarisation of our clay mud samples as suggested earlier by Obrien & Rowlands (1993) for kaolinite, Rasmusson *et al.* (1997) for montmorillonite and later by Revil and co-workers (e.g., Leroy & Revil, 2009; Revil 2012; Okay *et al.* 2014) for clayey materials. The f_Q values globally increase when salinity increases, especially for kaolinite and red montmorillonite at 1 M NaCl initially. Kaolinite presents also smaller f_Q values than illite and green and red montmorillonite. The obtained f_Q values are in accordance with the fact that kaolinite has a smaller structural charge than illite and

montmorillonite inducing potentially weaker ion adsorption in the Stern layer and higher sensitivity to bulk pore water chemical composition. Indeed, the presence of a strong structural charge on the basal surfaces of illite and montmorillonite particles induces a strong electrostatic force attracting and condensing counter-ions and water molecules in the Stern layer (Bourg & Sposito 2011) that may be weaker in the case of kaolinite particle carrying a weak structural charge on its silica basal surface (Leroy *et al.* 2024). As a consequence, Stern layer adsorption should be weaker and f_Q smaller in pure kaolinite sample than in pure illite and montmorillonite samples. In addition, a significant part of the surface of a kaolinite particle (edge and alumina basal surfaces) is occupied by silica and alumina hydroxyl surface sites (>Si-OH, >Al-OH) exchanging proton with Na^+ ion from bulk water in the Stern layer (Tombacz & Szekeres 2006). In that situation, the adsorption of Na^+ in the Stern layer increases the magnitude of the negative mineral surface charge density (Leroy & Revil 2004). Therefore, at fixed bulk pore water pH, increasing bulk water NaCl concentration increases H^+ to Na^+ exchange in the Stern layer and the magnitude of Q_0, leading to higher Na^+ adsorption in the Stern layer and potentially higher f_Q values for pure kaolinite. However, our kaolinite sample is not pure and contains significant amounts of smectite (4 %) and illite (3 %) presenting a high structural charge according to XRD measurements, therefore increasing and limiting the expected increase of f_Q with salinity. We also found that illite has higher f_Q values than montmorillonite when NaCl concentrations in bulk water are similar in accordance with the stronger surface charge density of illite (Q_0 = -0.190 C m^{-2}, Table 4) than montmorillonite (Q_0 = -0.168 C m^{-2} for green Mt and Q_0 = -0.171 C m^{-2} for red Mt, Table 4) inducing stronger Na^+ adsorption in the Stern layer. The evolution of f_Q values with salinity for montmorillonite is in agreement with the trend reported by Leroy *et al.* (2015). There is a slight decrease of f_Q at intermediate salinity that was also reported by Leroy *et al.* (2015),

due to the use of Na^+ activity coefficient of value below 1 in their Stern layer surface complexation model. At the highest salinity about 1 M NaCl, we, like Leroy *et al.* (2015), also observed the highest f_Q value. Nevertheless, we observed higher f_Q values than in Leroy *et al.* (2015) (they reported f_Q between 0.625 and 0.7 or 0.75 considering or not Na^+ activity coefficient). This can be explained by the higher amount of clay in our samples that favour higher Stern layer adsorption due to clay charged surfaces that are closer each to other.

Surface charge slows down counter-ions and water molecules on the clay surface (Greathouse *et al.* 2016). Kaolinite has a higher ion mobility ratio (mr_S) and effective ion mobility in the Stern layer (β_S) than montmorillonite, and montmorillonite has a higher β_S than illite, at similar salinity (Table 5). This can be explained by the fact that kaolinite has in theory a weaker structural charge than montmorillonite (Grim 1962), and montmorillonite has a weaker structural charge than illite (Ghasemi & Sharifi 2021). Nevertheless, our kaolinite sample is not pure and we did not have such weak surface charge density for it in our model (Q_0 = -0.324 C m^{-2}, Table 4). For illite, the mr_S value significantly decreases when salinity increases from 1.804×10^{-2} to 1.816×10^{-1} M NaCl. For red montmorillonite, we observe the same behaviour when salinity increases from 1.541×10^{-1} to 1.509 M NaCl (Table 5). We attribute this decrease of effective ion mobility in the Stern layer by the effect of increasing salinity and clay particle coagulation (Tombacz & Szekeres 2006). Clay particle coagulation should arrive earlier for illite than for montmorillonite because of the smaller surface area of illite where the structural charge inducing an EDL is expressed (Tournassat *et al.* 2015). Indeed, two similar clay particles with the same charged surface are repelled by each other due to the electrostatic diffuse layer force (Tombacz & Szekeres 2004). This electrostatic force weakens when salinity increases because of the compression of the diffuse layer leading to clay coagulation (Bouhaik *et al.* 2013). The larger the surface area is, the larger the

associated diffuse layer repulsive force is expressed between the two charged surfaces, and the larger is the salinity necessary to suppress it.

The number of stacked TOT sheets per particle, n_c, is 2 for the two montmorillonites at the two lower salinities, in agreement with the experimental observations of Schramm & Kwak (1982) on Na-Mt suspensions. At the highest salinity, we found $n_c = 25$ in agreement with the experimental observations of Michot *et al.* (2013) where they reported that about 30 TOT sheets are stacked per particle when Na-Mt particles strongly coagulate in 1 M $NaNO_3$ electrolyte. In our calculations, we used $n_c = 1$ for kaolinite and illite (Table 5), but, in reality, the number of sheets per particle according to our model is around 200 for kaolinite particles in kaolinite sample and around 6 for illite particles in illite sample (see supplementary material). These values are in the range of n_c expected values for kaolinite ($10 \leq n_c \leq 200$) and illite ($5 \leq n_c \leq 20$) particles (Leroy et *al.* 2024).

The cementation exponent *m*, which depends on the shape of the aggregates (Table S1 in supplementary material), globally increases when salinity increases. Compression of the diffuse layer and increasing particle coagulation when salinity increases can explain such results. The optimised *m* value is also higher for illite and montmorillonite than for kaolinite, for which our model predicts a spherical shape for the aggregates (*m* = 1.5; Table 5). Illite and montmorillonite have more elongated particles than kaolinite (Tournassat *et al.* 2015), which can explain such *m* values. These results showing in average increasing *m* values in the ascending order of kaolinite, illite and montmorillonite are in accordance with what was found previously by Leroy & Revil (2009) and Okay *et al.* (2014). However, these authors found higher *m* values with $m = 2$ for kaolinite, $m \in \{2,3\}$ for illite (only reported in Leroy & Revil (2009)) and $m \in \{3,4\}$ for smectite. The difference we obtained between Leroy & Revil (2009), Okay *et al.* (2014) and our model concerning the *m* values can be explained by the

fact that we consider here a polarising porous clay aggregate with an excess of charge per unit pore volume (Q_V) in agreement with Vinegar & Waxman (1984) and more recently with Leroy *et al.* (2017) – on the contrary to Leroy & Revil (2009) and Okay *et al.* (2014) who considered a polarising but not porous aggregate.

3.2.3 Output model parameter values (deduced from the model)

At low salinity (0.01 M NaCl initially), our model predicts that the diffuse layer occupies most of the connected pore space of illite and montmorillonite and controls diffuse layer conductivity σ_w^d and water conductivity σ_w (see Θ_w^d values in Table 6). At higher salinity (0.1 M NaCl initially), it predicts diffuse layer compression and that more connected pore space is occupied by bulk water, which controls bulk water conductivity σ_w^b and then σ_w (Tournassat & Appelo 2011). Even at 0.1 M NaCl, our model predicts that montmorillonite samples contain a significant pore water volume occupied by the diffuse layer. It should be noted that we consider that the montmorillonite interlayer space is filled by diffuse layer. Despite simulating diffuse layer compression, computed pore water volume fraction of the diffuse layer remains significant even at the highest salinity (1 M NaCl initially). Indeed the calculated interlayer space volume fraction over diffuse layer and interlayer space volume increases when initial NaCl concentration increases from 0.1 to 1 M NaCl (Ξ_i, Eq. 5, Table 6).

Table 6. Output model parameter values (not optimised) inferred from the computation of the complex conductivity of clay muds.

Clay	C_b M	σ_0 S m^{-1}	σ_w S m^{-1}	σ_w^b S m^{-1}	σ_w^d S m^{-1}	φ_d mV	Θ_w^d	Ξ_i	$10^8 B^d_{Na^+}$ m^2 s^{-1} V^{-1}	ϕ_a	$10^{-7} Q_V$ C m^{-3}
Kaolinite	0.015	0.297	0.326	0.171	4.875	-155.6	0.252	-	11.01	0.238	6.60
	0.191	1.632	1.790	1.595	7.046	-89.73	0.072	-	6.686	0.101	23.17
Illite	0.018	0.288	0.400	0.200	0.567	-75.31	0.658	-	7.664	0.555	4.188
	0.182	1.073	1.559	1.499	1.759	-30.71	0.242	-	4.405	0.283	13.24
Gr. Mt	0.015	0.555	0.591	0.164	0.591	-84.26	1.000	0.198	7.814	0.723	13.24
	0.146	1.625	1.726	1.197	1.883	-47.53	0.800	0.238	5.011	0.684	15.95
Red Mt	0.017	0.602	0.796	0.194	0.796	-90.06	1.000	0.214	8.425	0.706	14.70
	0.154	1.352	1.738	1.298	1.879	-43.50	0.783	0.243	4.972	0.679	16.67
	1.509	8.216	10.55	10.59	10.47	-13.34	0.378	0.960	3.048	0.507	34.29

Computed Na^+ ion mobility in the diffuse layer, $B^d_{Na^+}$, decreases when salinity increases. This results from (i) the mutual interaction of oppositely-charged ions that diminishes the mobility of Na^+ and Cl^- ($\beta^b_{Na^+}$ and $\beta^b_{Cl^-}$ respectively) (see Table S2 and Leroy *et al.* 2015) and (ii) the compression of the diffuse layer that causes a smaller increase of the diffuse layer conductivity due to electroosmosis (Dufreche *et al.* 2001 and Eqs 28-32). Magnitude of simulated electrical potential at the beginning of the diffuse layer, φ_d, decreases when salinity increases due to diffuse layer compression. The values we found for φ_d in the case of montmorillonite are in agreement with the values reported by Leroy *et al.* (2015) for the montmorillonite basal surface (Table 6). Illite has smaller calculated φ_d values than montmorillonite, in agreement with Horikawa *et al.* (1988) and Leroy & Revil (2009), due to stronger ion adsorption in the Stern layer (higher f_Q value, Table 5). The φ_d potentials we obtained for kaolinite may be too large compared to the φ_d potentials for illite and montmorillonite (Leroy & Revil 2004; Tombacz & Szekeres 2006). We attribute this result to the heterogeneity of our kaolinite sample, which contains significant solid contents of

smectite (4 %) and illite (3 %). In our model, the surprisingly large mineral surface charge density ($Q_0 = -0.324$ C m^{-2}) and low fractions of the counter-charge in the Stern layer ($f_Q = 0.52$ at 0.01 M NaCl initially and $f_Q = 0.53$ at 0.1 M NaCl initially) induce large φ_d potentials. Finally, we observe an increase of the excess of charge per unit pore volume in the aggregate (Q_V) when salinity increases, due to the decrease of the aggregate porosity ϕ_a (Table 6 and Eq. 15).

3.2.4 Comparison to the model of Weller et al. (2013)

The electrical formation factor F ($F \geq 1$) is an important petrophysical parameter in geophysics (e.g., Revil & Leroy 2004). It is defined by the ratio of water conductivity to saturated sample conductivity in absence of surface conductivity (Archie 1942), i.e.

$$F = \lim_{\sigma_s \to 0} \frac{\sigma_w}{\sigma'}. \tag{44}$$

Hence, $F = 1$ means that the current lines in water are not modified by the solid matrix and a high formation factor value like $F = 10$ means that the current lines in water are deformed by the solid matrix, thus decreasing sample capability to let current passing through the sample, and therefore its electrical conductivity. The electrical formation factor provides therefore paramount information on pore structure and investigated porous medium transport properties like ion diffusive properties and permeability (e.g., Revil & Cathles 1999; Leroy *et al.* 2006; Jougnot *et al.* 2009; Revil & Florsch 2010; Al Khalifah *et al.* 2020; Peshtani *et al.*, 2024). In addition, Archie (1942) in his first law showed that the electrical formation factor can be computed from sample porosity ϕ and cementation exponent *m* when surface conductivity can be neglected, i.e.

$$F = \phi^{-m}. \quad (45)$$

It is usually assumed that it is very difficult to determine the formation factor of clays such as montmorillonite because of the high conductivity on their surface compared to bulk water conductivity (Revil *et al.* 1998; Leroy & Revil 2009; Weller *et al.* 2013). For argillites and mudstones, it is also difficult to determine F given how low the permeability is and how difficult it is to saturate such tight pore spaces (Neuzil, 1994; Jougnot *et al.* 2010a; Peshtani *et al.* 2024). To reduce the effect of surface conductivity, it is common to increase the water conductivity (de Lima & Sharma 1992; Weller *et al.* 2013; Li *et al.* 2016). But in the case of clay muds, this changes their structure because of diffuse layer compression (Leroy *et al.* 2017; Okay *et al.* 2014). In addition, in the case of nanoporous clays such as montmorillonite, it is very difficult to estimate accurately water conductivity, because of the presence of the diffuse layer and interlayer space filling a significant part of the pores (Leroy & Revil 2009).

To quantify the surface conductivity contribution, we used the Dukhin number, defined by $Du = \left|\sigma_s^* / \sigma_w^*\right|$. In our samples, it is less than 0.1 (Fig. 9), meaning that in our model the surface conductivity contribution (due to the Stern layer) to the measured magnitude of sample conductivity can be neglected. Therefore Archie's first law should apply here.

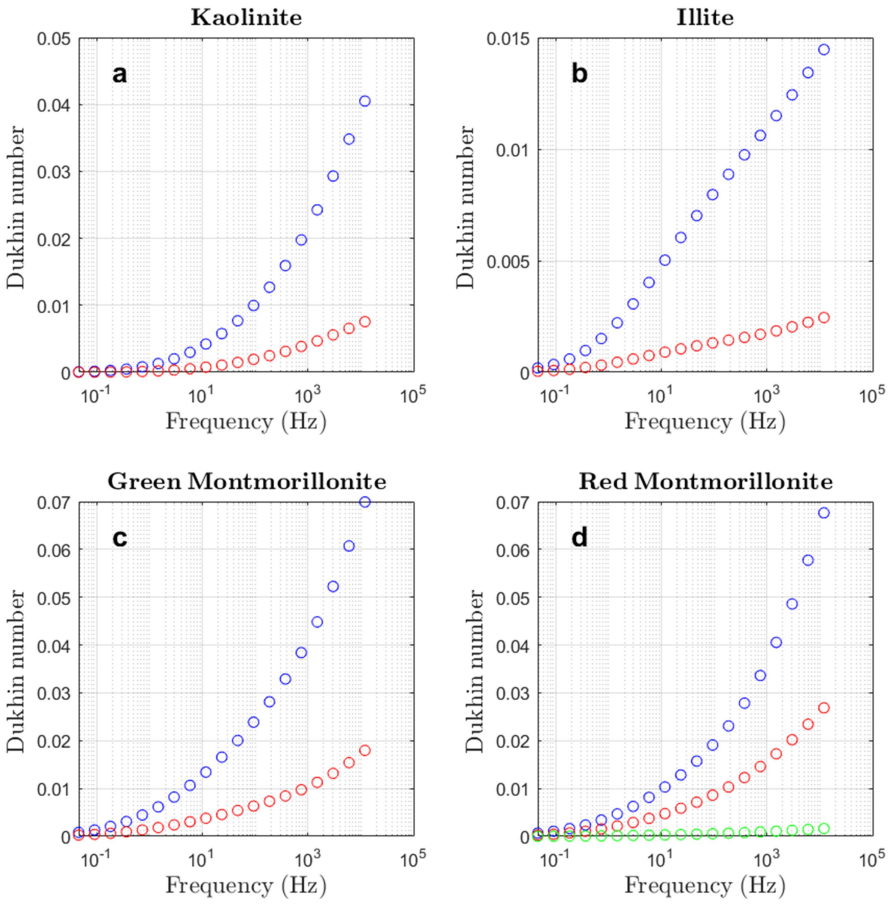

Figure 9. Dukhin number as a function of frequency and salinity. Blue: 0.01 M NaCl, red: 0.1 M NaCl, and green: 1 M NaCl initially.

Our model allows us to estimate the electrical formation factor of our clay muds in the two ways presented previously (Eqs 44 and 45). For that purpose we chose in-phase conductivity measurements on clay muds (σ') at low frequency (here 1.46 Hz) where surface conductivity effect on in-phase conductivity measurements can be neglected. It should be noted again that in our model the diffuse layer only contributes to water conductivity and not to surface conductivity according to O'Konski (1960) because the diffuse layer can be thicker than the particle (see related discussion in section 3 of Leroy *et al.* 2024). Water conductivity (σ_w) and mud porosity (ϕ) were computed using the method outlined in Section 2. The cementation exponent m was obtained by optimisation (Section 2.1).

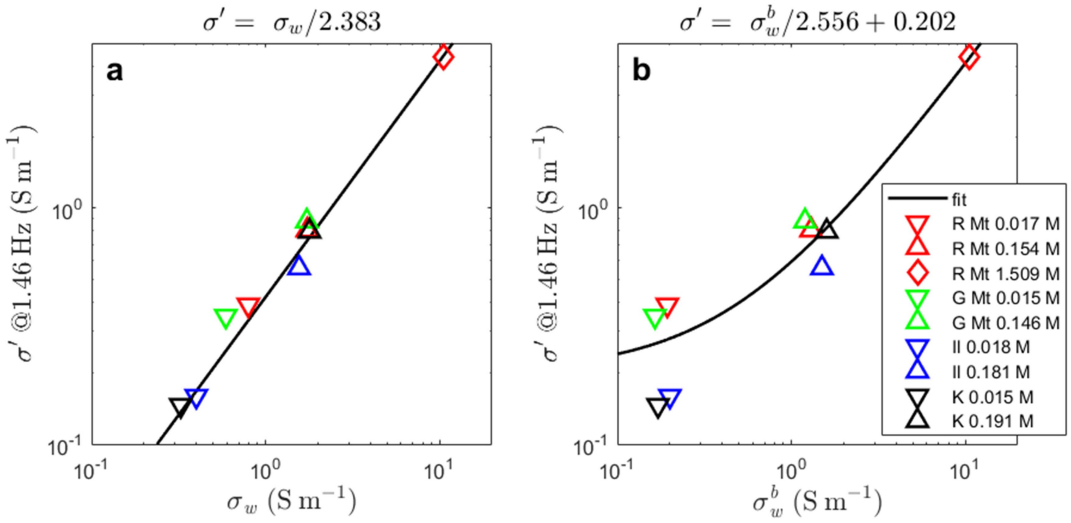

Figure 10. Measured in-phase conductivity of the samples at a frequency of 1.46 Hz as a function of the computed water conductivity (**a**) and measured in-phase conductivity of the samples at a frequency of 1.46 Hz as a function of the computed bulk water conductivity (**b**).

Fig. 10a shows that first Archie's law (represented here by Eq 44) can indeed be used to interpret in-phase conductivity measurements on clay muds at low frequency (typically ≤ 1 Hz) when clay water conductivity is computed considering the diffuse layer contribution. However, first Archie's law cannot be used to interpret in-phase conductivity measurements on clay muds at low frequency when only bulk water conductivity is known because σ_w^b underestimates clay water conductivity especially at low salinity (0.01 M NaCl initially) (Fig10b and 11). It is therefore necessary to consider surface conductivity in parallel to bulk conductivity to explain in-phase conductivity measurements at low frequency when using bulk water conductivity only. For instance, Weller *et al.* (2013) considered $\sigma' = \sigma_w^b / F + \sigma_s'$ to explain in-phase conductivity measurements at low frequency on clayey materials.

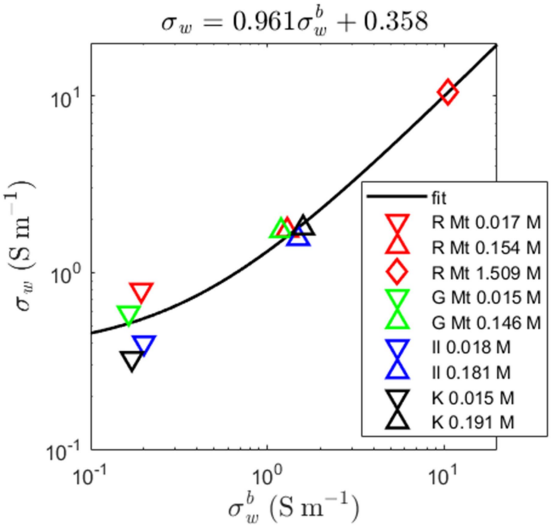

Figure 11. Computed water conductivity versus computed bulk water conductivity.

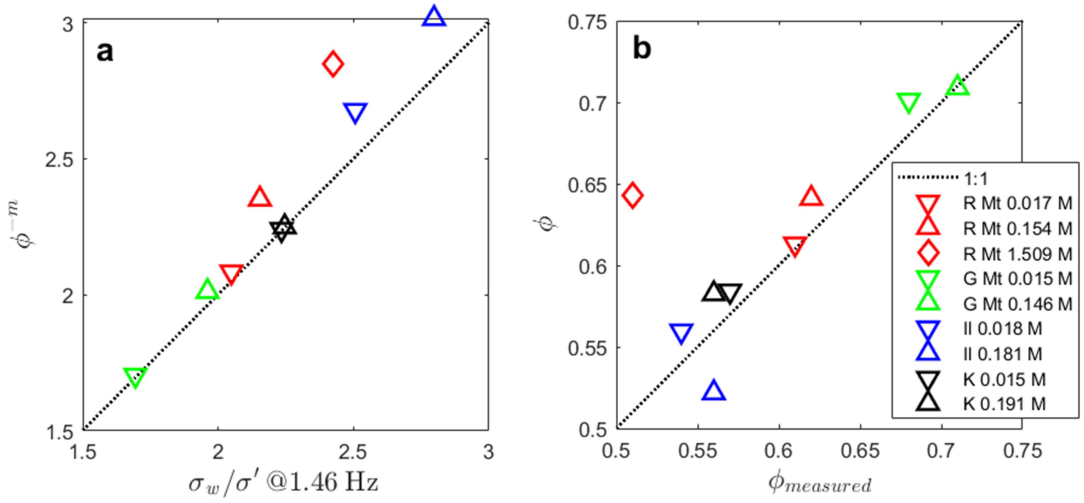

Figure 12. Electrical formation factor deduced from the model ($F = \phi^{-m}$) compared to the electrical formation factor deduced from the model and the measurement ($F = \sigma_w / \sigma'(1.46\ \text{Hz})$) (**a**). Calculated porosity versus measured porosity (**b**).

Table 7. Computed clay mud porosity (ϕ) and measured porosity of the sample (ϕ_{meas}) (from *Mendieta et al.* [2021]).

Clays	Kaol.	Kaol.	Illite	Illite	G. Mt	G. Mt	R. Mt	R. Mt	R. Mt
C_b (M)	0.0154	0.1908	0.0180	0.1816	0.0153	0.1457	0.0171	0.1541	1.5091
ϕ	0.584	0.583	0.560	0.522	0.701	0.709	0.613	0.641	0.643
ϕ_{meas}	0.57	0.56	0.54	0.56	0.68	0.71	0.61	0.62	0.51

The predictions of the electrical formation factor using $F = \phi^{-m}$ are in relative agreement with the experimental measurements using $F = \sigma_w / \sigma'(@1.46\,\text{Hz})$ (Fig. 11a). Most F discrepancies are observed for illite at 0.1 M NaCl initially and red montmorillonite at 1 M NaCl initially where particle coagulation occurs. It should be noted that our model using $F = \phi^{-m}$ reproduces very well the corresponding "observed" F measurements when using m = 1.5 in our computations (spherical aggregates) and that our F prediction discrepancy from the "observed" one increases when m increases (Table 5). Computed clay mud porosities are also in agreement with the related measurements reported in Mendieta *et al.* (2021) except for the clay mud porosity of red montmorillonite at 1 M NaCl initially, which is surprisingly low ($\phi \cong 0.51$) compared to the other clay mud porosity measurements ($\phi \cong 0.61$ in average) and the model prediction ($\phi \cong 0.64$) (Figs 12b and Table 7). We can attribute this observed porosity difference by the fact that we considered that the interlayer space of red Mt contributes to sample porosity whereas this type of porosity was not measured during the experiment of Mendieta *et al.* (2021). It is not surprising that the clay mud porosities computed by our model are in agreement with the corresponding measurements because we know the mass of clay powder in our model (δ_s), the solid volumetric mass density (ρ_s) ($\rho_s \cong 2700$ kg m^{-3}), and the sample volume (V_t). Indeed:

$$\phi = \frac{V_w}{V_t} = \frac{V_t - 10^6 V_s}{V_t} = \frac{V_t - 10^3 \delta_s / \rho_s}{V_t}. \quad (46)$$

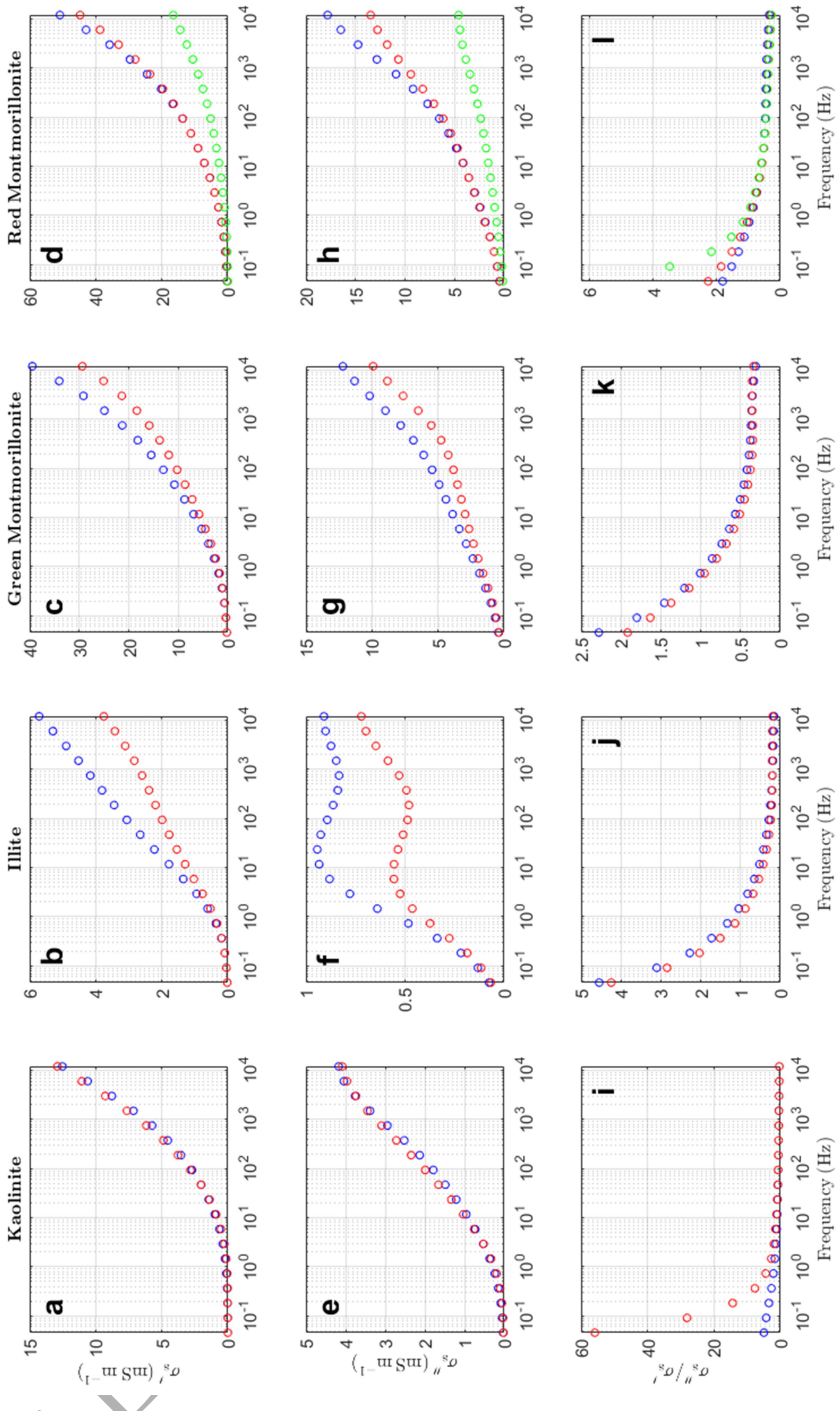

Figure 13. Real part (**a-d**) and imaginary part (**e-h**) of the surface conductivity of the clay samples at different salinities as a function of frequency. Ratio of the imaginary part to the real part of the surface conductivity of the clay samples at different salinities as a function of frequency (**i-l**). Blue: 0.01 M NaCl, red: 0.1 M NaCl, and green: 1 M NaCl initially.

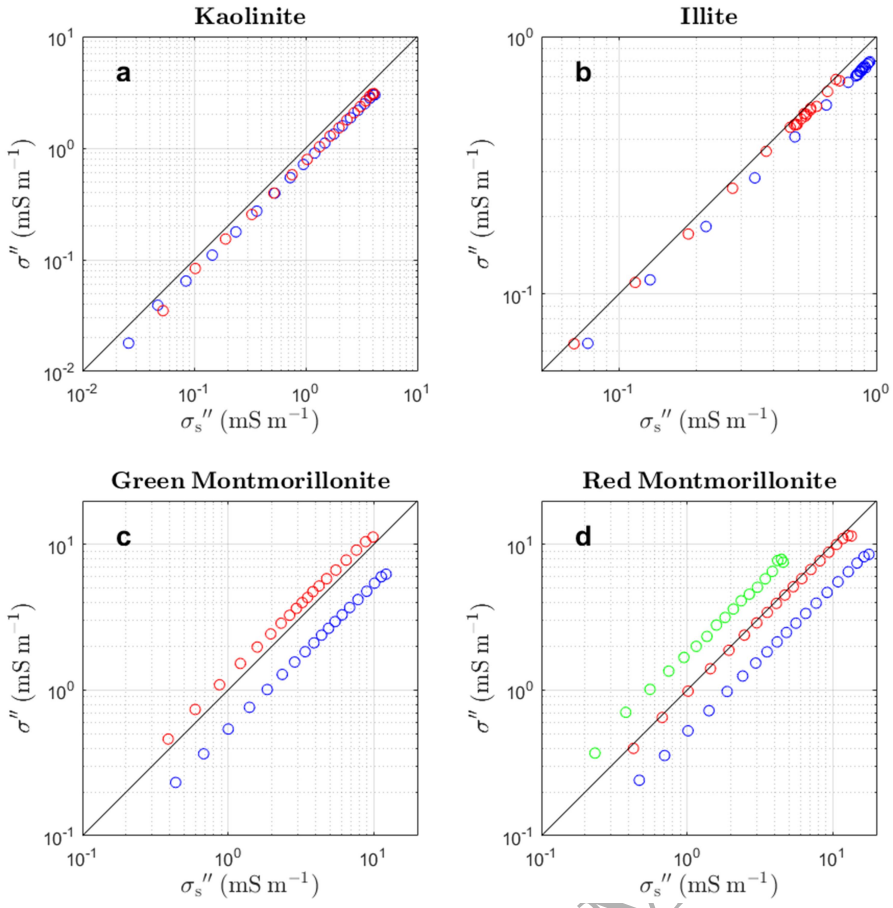

Figure 14. Measured sample quadrature conductivity as a function of the imaginary part of surface conductivity at different salinities (blue: 0.01 M NaCl, red: 0.1 M NaCl, and green: 1 M NaCl initially).

Our model can also be used to determine the surface conductivity of clay aggregates $\sigma_s^* = \sigma_s' + i\sigma_s''$ (Eq 22). Fig. 13 shows modelled σ_s' and σ_s'', with σ_s' being stronger in magnitude than σ_s'' for frequency above 1 Hz. Weller *et al.* (2013) considered that the EDL on clay particle surface controls surface conductivity. They introduced the parameter $l = \sigma_s''/\sigma_s'$. Our modelled l ratio strongly decreases when the frequency increases in particular at low frequencies due to the high increase of σ_s' when frequency increases (Fig. 13). It is also sensitive to salinity, especially for frequencies below 1 Hz. Our modelling results also show that computed surface quadrature conductivity σ_s'' is not equal to the

measured sample quadrature conductivity σ'' (Fig. 14). Indeed, we found that $\sigma'' = a\sigma_s''$ with *a* being a real constant, which is not necessarily equal to 1, contrary to what was assumed by Weller *et al.* (2013). Furthermore, the slope *a* increases when salinity increases, especially for montmorillonite. Such results can be explained by the self-consistent model used here (BHS model) to compute mud conductivity from surface and water conductivities in the case of very low Dukhin number (Fig. 9) and large contribution of the diffuse layer and interlayer space of Na-Mt to water conductivity (Table 6).

4 CONCLUSIONS AND PERSPECTIVES

We have developed a new methodology to explain laboratory spectral induced polarisation (SIP) measurements on kaolinite, illite, and montmorillonite concentrated muds at different NaCl concentrations, using a mechanistic model taking into account microstructural and electrochemical properties. The model considers explicitly the influence of the mobile ions in the electrical double layer (EDL) covering clay particle external surfaces and in the interlayer space of montmorillonite on complex conductivity. We assume that the diffuse layer contributes to water conductivity and not to surface conductivity because the diffuse layer can be thicker than the clay particle. In our model, the counter-ions in the Stern layers around interacting clay particles, which form aggregates, and the mobile counter-ions in the interlayer space of montmorillonite particles control the electrochemical polarisation and the surface conductivity. One limitation of our model is that it does not take into account full diffuse layer polarisation as well as the polarisation due diffuse layer interaction, which can lead to a membrane-like polarisation effect – a further work in that direction would be therefore necessary to complete our approach.

Distribution of relaxation times is first inverted from the measured SIP spectra using the

Debye decomposition approach. It serves to get the partial chargeability distribution and then the effective size distribution of the clay aggregates. Afterwards an optimization procedure is used to adjust the parameters of the model by comparing model predictions to measured SIP spectra for each type of clay at different salinities (NaCl). These parameters are the fraction of the counter-charge and the effective ion mobility (tangentially to the clay surface) of Na^+ counter-ions in the Stern layer, the number of stacked sheets per montmorillonite particle, and the cementation exponent of the aggregates characterising their shape.

Our model is able to reproduce rather well the measured SIP spectra of concentrated clay muds using optimised parameter values, in agreement with the corresponding data reported in the physical-chemistry literature, except for two parameters: the effective size distribution of the clay aggregates and the effective ion mobility in the Stern layer. As mentioned, these parameters are effective ones. Due to the large concentration of interacting clay particles in the investigated samples (typically around 1 thousand grams of solid clay powder per litre of sample) compared to clay dispersions (particle concentration typically below 1 hundred grams of solid clay powder per litre of sample), it was not possible to estimate accurately the size distribution of the aggregates from measured SIP spectra and to use directly the ion mobility values deduced from molecular dynamic simulations, which are significantly too high.

Our approach suggests that most of the EDL counter-charge controlling SIP spectra on clayey materials is located in the Stern layer, especially on the basal surface of illite and montmorillonite. We also obtained a very low value for the effective ion mobility of Na^+ counter-ions in the Stern layer, between one and two orders of magnitude below the corresponding ion mobility in bulk and distilled water (but in agreement with values reported in the geophysical literature). The numbers of stacked montmorillonite sheets per particle are in agreement with the values reported in the physical-chemistry literature including when particle coagulation occurs. In our model, clay aggregates have spherical and spheroidal

shapes and their elongation increases when salinity increases for montmorillonite.

We showed that first Archie's law can be used to explain in-phase conductivity measurements at low frequency (typically ≤ 1 Hz) on clayey materials when water conductivity can be modelled to include the contribution of the diffuse layer. We also extracted surface conductivity from measured SIP spectra and reported their dependence on salinity and frequency for each type of clay. We found that the ratio of the imaginary part of surface conductivity to its real part is highly dependent on frequency and can also depend on salinity at frequencies below 1 Hz. Finally, we observed from our model that the measured quadrature conductivity is proportional, but not identical, to the imaginary part of surface conductivity.

It would be interesting to use our approach to infer the state and transport properties of unconsolidated and consolidated clay materials from SIP spectra. Among them, clay content, bulk water salinity, ion diffusivity and permeability would be of particular importance. In addition, our results should be confirmed using purely numerical SIP models developed at the scale of the clay particle combined with high resolution imaging techniques.

ACKNOWLEDGMENTS

This study was carried out within the framework of the ANR EXCITING and IMAGE projects (grants ANR-17-CE06-0012 and ANR-21-CE04-0013, respectively, funded by the French National Research Agency). Philippe Leroy warmly thanks Francis Claret for his support and Sylvain Grangeon for the fruitful discussions. The work of Philippe Leroy was also supported by the EURAD work package DONUT (EC grant agreement No. 847593). We thank the editor, Léa Levy, Klaudio Peshtani and an anonymous referee for reviewing our manuscript.

DATA AVAILABILITY STATEMENT

The data used in this study are available in the Zenodo repository (http://doi.org/10.5281/zenodo.4050345).

REFERENCES

Al Khalifah, H., Glover, P. W. J. & Lorinczi, P., 2020. Permeability prediction and diagenesis in tight carbonates using machine learning techniques, *Marine and Petroleum Geology*, **112**, 104096, doi:10.1016/j.marpetgeo.2019.104096.

Ali, E. S., Askalany, A. A., Harby, K., Diab, M. R., Hussein, B. R. M. & Alsaman, A. S., 2021. Experimental adsorption water desalination system utilizing activated clay for low grade heat source applications, *Journal of Energy Storage*, **43**, 103219, doi:10.1016/j.est.2021.103219.

Anderson, R. L., Ratcliffe, I., Greenwell, H. C., Williams, P. A., Cliffe, S. & Coveney, P. V., 2010. Clay swelling — A challenge in the oilfield, *Earth-Science Reviews*, **98**(3-4), 201-216, doi:10.1016/j.earscirev.2009.11.003.

Archie, G. E., 1942. The electrical resistivity log as an aid in determining some reservoir characteristics, *Transactions of the American Institute of Mining, Metallurgical & Petroleum Engineers*, **146**, 54-67.

Bergaya, F. & Vayer, M., 1997. CEC of clays: Measurement by adsorption of a copper ethylenediamine complex, *Applied Clay Science*, **12**(3), 275-280, doi:10.1016/s0169-1317(97)00012-4.

Binley, A., Hubbard, S. S., Huisman, J. A., Revil, A., Robinson, D. A., Singha, K. & Slater, L. D., 2015. The emergence of hydrogeophysics for improved understanding of subsurface processes over multiple scales, *Water Resources Research*, **51**(6), 3837-3866, doi:10.1002/2015WR017016.

Börner, F., Gruhne, M. & Schön, J., 1993. Contamination Indications Derived from Electrical-Properties in the Low-Frequency Range, *Geophysical Prospecting,* **41,** 83-98, doi:10.1111/j.1365-2478.1993.tb00566.x.

Bouhadja, M. & Skelton, A. A., 2018. Dynamical Properties of Water and Ions at the Quartz (101)–Water Interface at a Range of Solution Conditions: A Classical Molecular Dynamics Study, *The Journal of Physical Chemistry C*, **122**(3), 1535-1546, doi:10.1021/acs.jpcc.7b08214.

Bouhaik, I. S., Leroy, P., Ollivier, P., Azaroual, M. & Mercury, L., 2013. Influence of surface conductivity on the apparent zeta potential of TiO2 nanoparticles: Application to the modeling of their aggregation kinetics, *Journal of Colloid and Interface Science*, **406**, 75-85, doi:10.1016/j.jcis.2013.05.034.

Bourg, I. C., Bourg, A. C. M. & Sposito, G., 2003. Modeling diffusion and adsorption in compacted bentonite: a critical review, *Journal of Contaminant Hydrology*, **61**(1-4), 293-302, doi:10.1016/s0169-7722(02)00128-6.

Bourg, I. C. & Sposito, G., 2011. Molecular dynamics simulations of the electrical double layer on smectite surfaces contacting concentrated mixed electrolyte (NaCl-CaCl2) solutions, *Journal of Colloid and Interface Science*, **360**(2), 701-715,

doi:10.1016/j.jcis.2011.04.063.
Bristow, T. F., et al., 2018. Clay mineral diversity and abundance in sedimentary rocks of Gale crater, Mars, *Science Advances*, **4**(6), eaar3330, doi:10.1126/sciadv.aar3330.
Bücker, M., Flores Orozco, A., Undorf, S. & Kemna, A., 2019. On the Role of Stern- and Diffuse-Layer Polarization Mechanisms in Porous Media, *Journal of Geophysical Research: Solid Earth*, **124**, 5656-5677, doi:10.1029/2019jb017679.
Chaaya, R., Gaboreau, S., Milet, F., Maubec, N., Tremosa, J., Raimbourg, H. & Ferrage, E., 2023. In-operando X-ray scattering characterization of smectite swelling experiments, *Applied Clay Science*, **245**, 107124, doi:10.1016/j.clay.2023.107124.
Coussot, P. & Piau, J. M., 1994. On the behavior of fine mud suspensions, *Rheologica Acta,* **33,** 175-184, doi:10.1007/bf00437302.
de Lima, O. A. L. & Sharma, M. M., 1992. A generalized Maxwell-Wagner theory for membrane polarization in shaly sands, *Geophysics*, **57**(3), 431-440, doi:10.1190/1.1443257.
Dufreche, J. F., Marry, V., Bernard, O. & Turq, P., 2001. Models for electrokinetic phenomena in montmorillonite, *Colloids and Surfaces A - Physicochemical and Engineering Aspects*, 1**95**(1-3), 171-180, doi:10.1016/S0927-7757(01)00840-8.
Ewis, D., Ba-Abbad, M. M., Benamor, A. & El-Naas, M. H., 2022. Adsorption of organic water pollutants by clays and clay minerals composites: A comprehensive review, *Applied Clay Science*, **229**, 106686, doi:10.1016/j.clay.2022.106686.
Florsch, N., Revil, A. & Camerlynck, C., 2014. Inversion of generalized relaxation time distributions with optimized damping parameter, Journal of Applied Geophysics, **109**, 119132, doi:10.1016/j.jappgeo.2014.07.013.
García-Romero, E., Lorenzo, A., García-Vicente, A., Morales, J., García-Rivas, J. & Suárez, M., 2021. On the structural formula of smectites: a review and new data on the influence of exchangeable cations, *Journal of Applied Crystallography*, **54**(1), 251-262, doi:10.1107/s1600576720016040.
Garrels, R. M. & Mackenzie, F. T., 1971. Evolution of sedimentary rocks, W.W. Norton and Co, New York, 397 pp.
Gehin, A., Greneche, J. M., Tournassat, C., Brendle, J., Rancourt, D. G. & Charlet, L., 2007. Reversible surface-sorption-induced electron-transfer oxidation of Fe(II) at reactive sites on a synthetic clay mineral, *Geochimica et Cosmochimica Acta*, **71**(4), 863-876, doi:10.1016/j.gca.2006.10.019.
Ghasemi, M. & Sharifi, M., 2021. Effects of layer-charge distribution on swelling behavior of mixed-layer illite-montmorillonite clays: A molecular dynamics simulation study, *Journal of Molecular Liquids*, **335**, 116188, doi:10.1016/j.molliq.2021.116188.
Greathouse, J. A., Cygan, R. T., Fredrich, J. T. & Jerauld, G. R., 2016. Molecular Dynamics Simulation of Diffusion and Electrical Conductivity in Montmorillonite Interlayers, *The Journal of Physical Chemistry C*, **120**(3), 1640-1649, doi:10.1021/acs.jpcc.5b10851.
Grim, R. E., 1962. Applied Clay Mineralogy, McGraw-Hill, New York, 422 pp.
Guisseau, D., Mas, P. P., Beaufort, D., Girard, J. P., Inoue, A., Sanjuan, B., Petit, S., Lens, A. & Genter, A., 2007. Significance of the depth-related transition montmorillonite-beidellite in the Bouillante geothermal field, Guadeloupe, Lesser Antilles. *American Mineralogist*, **92**(11-12), 1800-1813, doi:10.2138/am.2007.2398.
Hashin, Z. & Shtrikman, S., 1962. A Variational Approach to the Theory of the Effective Magnetic Permeability of Multiphase Materials, *Journal of Applied Physics*, **33**(10), 3125-3131, doi:10.1063/1.1728579.
Hassan, M. S., Villieras, F., Gaboriaud, F. & Razafitianamaharavo, A., 2006. AFM and low-pressure argon adsorption analysis of geometrical properties of phyllosilicates,

Journal of Colloid and Interface Science, **296,** 614-623, doi:10.1016/j.jcis.2005.09.028.

Horikawa, Y., Murray, R. S. & Quirk, J. P., 1988. The effect of electrolyte concentration on the zeta potentials of homoionic montmorillonite and illite, *Colloid Surface*, **32**, 181-195, doi:10.1016/0166-6622(88)80015-5.

Huisman, J. A., Zimmermann, E., Esser, O., Haegel, F.-H., Treichel, A. & Vereecken, H., 2016. Evaluation of a novel correction procedure to remove electrode impedance effects from broadband SIP measurements, *Journal of Applied Geophysics,* **135,** 466-473, doi:10.1016/j.jappgeo.2015.11.008.

Ingeman-Nielsen, T. & Baumgartner, F., 2006. CR1Dmod: A Matlab program to model 1D complex resistivity effects in electrical and electromagnetic surveys, *Computers & Geosciences*, **32**(9), 1411-1419, doi:10.1016/j.cageo.2006.01.001.

Jiang, T., Wu, Y., Liu, C., Whittle, A. J., Guo, D. & Zhang, G., 2022. Kinetics of flocculated illite suspensions affected by ionic strength, pH, and hydrodynamic shearing, *Applied Clay Science*, **221**, 106462, doi:10.1016/j.clay.2022.106462.

Jougnot, D., Revil, A., Lu, N. & Wayllace, A., 2010a. Transport properties of the Callovo-Oxfordian clay rock under partially saturated conditions, *Water Resources Research*, **46**(8), W08514, doi:10.1029/2009WR008552

Jougnot, D., Ghorbani, A., Revil, A., Leroy, P. & Cosenza, P., 2010b. Spectral induced polarization of partially saturated clay-rocks: a mechanistic approach, *Geophysical Journal International*, **180**(1), 210-224, doi:10.1111/j.1365-246X.2009.04426.x.

Jougnot, D., Revil, A. & Leroy, P., 2009. Diffusion of ionic tracers in the Callovo-Oxfordian clay-rock using the Donnan equilibrium model and the formation factor, *Geochimica Et Cosmochimica Acta,* **73,** 2712-2726, doi:10.1016/j.gca.2009.01.035

Kausar, A., Iqbal, M., Javed, A., Aftab, K., Nazli, Z.-i.-H., Bhatti, H. N. & Nouren, S., 2018. Dyes adsorption using clay and modified clay: A review, *Journal of Molecular Liquids*, **256**, 395-407, doi:10.1016/j.molliq.2018.02.034.

Kemna, A., Binley, A., Cassiani, G., Niederleithinger, E., Revil, A., Slater, L., Williams, K.H., Flores Orozco, A., Haegel, F.-H., Hördt, A., Kruschwitz, S., Leroux, V., Titov K. & Zimmermann, E., 2012. An overview of the spectral induced polarization method for near-surface applications, *Near Surface Geophysics*, **10**(6), 453-468, doi: 10.3997/1873-0604.2012027.

Khaldoun, A., Moller, P., Fall, A., Wegdam, G., De Leeuw, B., Méheust, Y., Otto Fossum, J. & Bonn, D. 2009. Quick Clay and Landslides of Clayey Soils, *Physical Review Letters*, **103**(18), doi:10.1103/PhysRevLett.103.188301.

Leroy, P., Maineult, A., Mendieta, A. & Jougnot, D., 2024. A mechanistic model for the complex conductivity of clay materials. I. Theory, submitted to *Geophysical Journal International*.

Leroy, P. & Revil, A., 2004. A triple-layer model of the surface electrochemical properties of clay minerals, *Journal of Colloid and Interface Science*, **270**(2), 371-380, doi:10.1016/j.jcis.2003.08.007.

Leroy, P. & Revil, A. 2009. A mechanistic model for the spectral induced polarization of clay materials, *Journal of Geophysical Research - Solid Earth*, **114**, B10202, doi:10.1029/2008jb006114.

Leroy, P., Revil, A., Altmann, S. & Tournassat, C., 2007. Modeling the composition of the pore water in a clay-rock geological formation, Callovo-Oxfordian, France, *Geochimica et Cosmochimica Acta*, **71**(5), 1087-1097, doi:10.1016/j.gca.2006.11.009.

Leroy, P., Revil, A. & Coelho, D., 2006. Diffusion of ionic species in bentonite, *Journal of Colloid and Interface Science*, **296**(1), 248-255, doi:10.1016/j.jcis.2005.08.034.

Leroy, P., Tournassat, C., Bernard, O., Devau, N. & Azaroual, M., 2015. The electrophoretic

mobility of montmorillonite. Zeta potential and surface conductivity effects, *Journal of Colloid and Interface Science*, **451**, 21-39, doi:10.1016/j.jcis.2015.03.047.
Leroy, P., Weigand, M., Mériguet, G., Zimmermann, E., Tournassat, C., Fagerlund, F., Kemna, A. & Huisman, J. A., 2017. Spectral induced polarization of Na-montmorillonite dispersions, *Journal of Colloid and Interface Science*, **505**, 1093-1110, doi:10.1016/j.jcis.2017.06.071.
Li, S., Leroy, P., Heberling, F., Devau, N., Jougnot, D. & Chiaberge, C., 2016. Influence of surface conductivity on the apparent zeta potential of calcite, *Journal of Colloid and Interface Science,* **468,** 262-275, doi:10.1016/j.jcis.2016.01.075.
Li, Z., Dong, M., Li, S. & Huang, S., 2006. CO2 sequestration in depleted oil and gas reservoirs—caprock characterization and storage capacity, *Energy Conversion and Management*, **47**(11-12), 1372-1382, doi:10.1016/j.enconman.2005.08.023.
Lyklema, J., Dukhin, S. S. & Shilov, V. N., 1983. The relaxation of the double-layer around colloidal particles and the low-frequency dielectric-dispersion. Part I. Theoretical Considerations, Journal of Electroanalytical Chemistry, **143**(1-2), 1-21, doi:10.1016/S0022-0728(83)80251-4.
Lyklema, J. & Minor, M., 1998. On surface conduction and its role in electrokinetics, *Colloids and Surfaces A - Physicochemical and Engineering Aspects*, **140**(1-3), 33-41, doi:10.1016/S0927-7757(97)00266-5.
Ma, C. & Eggleton, R. A., 1999. Cation Exchange Capacity of Kaolinite, *Clays and Clay Minerals*, **47**(2), 174-180, doi:10.1346/ccmn.1999.0470207.
Maineult, A., 2016. Estimation of the electrical potential distribution along metallic casing from surface self-potential profile, *Journal of Applied Geophysics*, **129**, 66-78, doi:10.1016/j.jappgeo.2016.03.038.
Malusis, M. A., Shackelford, C. D. & Olsen, H. W., 2003. Flow and transport through clay membrane barriers, *Engineering Geology*, **70**(3-4), 235-248, doi:10.1016/s0013-7952(03)00092-9.
Massat, L., Cuisinier, O., Bihannic, I., Claret, F., Pelletier, M., Masrouri, F. & Gaboreau, S., 2016. Swelling pressure development and inter-aggregate porosity evolution upon hydration of a compacted swelling clay, Applied Clay Science, **124-125**, 197-210, doi:10.1016/j.clay.2016.01.002.
Mendelson, K. S. & Cohen, M. H., 1982. The effect of grain anisotropy on the electrical-properties of sedimentary-rocks, *Geophysics*, **47**(2), 257-263, doi:10.1190/1.1441332.
Mendieta, A., Jougnot, D., Leroy, P. & Maineult, A., 2021. Spectral Induced Polarization Characterization of Non-Consolidated Clays for Varying Salinities—An Experimental Study, *Journal of Geophysical Research - Solid Earth*, **126**(4), e2020JB021125, doi:10.1029/2020jb021125.
Metz, V., Raanan, H., Pieper, H., Bosbach, D. & Ganor, J., 2005. Towards the establishment of a reliable proxy for the reactive surface area of smectite, *Geochimica et Cosmochimica Acta*, **69**(10), 2581-2591, doi:10.1016/j.gca.2004.11.009.
Michot, L. J., Bihannic, I., Thomas, F., Lartiges, B. S., Waldvogel, Y., Caillet, C., Thieme, J., Funari, S. S. & Levitz, P., 2013. Coagulation of Na-Montmorillonite by Inorganic Cations at Neutral pH. A Combined Transmission X-ray Microscopy, Small Angle and Wide Angle X-ray Scattering Study, Langmuir, **29**(10), 3500-3510, doi:10.1021/La400245n.
Neuzil, C. E., 1994. How permeable are clays and shales?, *Water Resources Research*, **30**(2), 145-150, doi:10.1029/93wr02930.
Obrien, R. W. & Rowlands, W. N., 1993. Measuring the Surface Conductance of Kaolinite Particles, *Journal of Colloid and Interface Science*, **159**(2), 471-476. doi:10.1006/jcis.1993.1348

O'Konski, C. T., 1960. Electric properties of macromolecules. V. Theory of ionic polarization in polyelectrolytes, *The Journal of Physical Chemistry*, **64**(5), 605-619, doi:10.1021/j100834a023.

Okay, G., Leroy, P., Ghorbani, A., Cosenza, P., Camerlynck, C., Cabrera, J., Florsch, N. & Revil, A., 2014. Spectral induced polarization of clay-sand mixtures: Experiments and modeling, *Geophysics*, **79**(6), E353-E375, doi:10.1190/Geo2013-0347.1.

Olhoeft, G. R., 1981. Electrical properties of rocks, in: *Physical properties of rocks and minerals*, edited by Touloukian, W. R. J. Y. S. & Roy R. F., pp. 257–339, McGraw-Hill, New York.

Pelton, W. H., Ward, S. H., Hallof, P. G., Sill, W. R. & Nelson, P. H., 1978. Mineral Discrimination and Removal of Inductive Coupling with Multifrequency-Ip, *Geophysics,* **43,** 588-609, doi:10.1190/1.1440839.

Peshtani, K., Weller, A. & Slater, L., 2024. Permeability and Induced Polarization of Mudstones, *Water Resources Research*, **6**(8), e2024WR037455, doi:10.1029/2024wr037455.

Porté, J., Bretaudeau, F. & Girard, J. F., 2023. 3-D complex resistivity imaging using controlled source electromagnetic data: a multistage procedure using a second order polynomial parametrization, *Geophysical Journal International,* **233,** 839-860, doi:10.1093/gji/ggac486.

Qi, Y. & Wu, Y., 2022. Electrical Conductivity of Clayey Rocks and Soils: A Non-Linear Model, *Geophysical Research Letters*, **49**(10), e2021GL097408, doi:10.1029/2021gl097408.

Qi, Y. & Wu, Y., 2024. Induced Polarization of Clayey Rocks and Soils: Non-Linear Complex Conductivity Models, *Journal of Geophysical Research - Solid Earth*, **129**(3), e2023JB028405, doi:10.1029/2023jb028405.

Rasmusson, M., Rowlands, W., OBrien, R. W. & Hunter, R. J., 1997. The dynamic mobility and dielectric response of sodium bentonite, *Journal of Colloid and Interface Science*, **189**(1), 92-100, doi:10.1006/jcis.1997.4793.

Revil, A., 2012. Spectral induced polarization of shaly sands: Influence of the electrical double layer, *Water Resources Research*, **48**(2), W02517, doi:10.1029/2011WR011260.

Revil, A. & Florsch, N., 2010. Determination of permeability from spectral induced polarization in granular media, *Geophysical Journal International,* **181,** 1480-1498, doi:10.1111/j.1365-246X.2010.04573.x.

Revil, A., Cathles, L. M., Losh, S. & Nunn, J. A., 1998. Electrical conductivity in shaly sands with geophysical applications, *Journal of Geophysical Research - Solid Earth*, **103**(B10), 23925-23936, doi:10.1029/98JB02125.

Revil, A. & Cathles, L. M., 1999. Permeability of shaly sands, *Water Resources Research*, **35**(3), 651-662, doi:10.1029/98wr02700.

Revil, A. & Glover, P. W. J., 1997. Theory of ionic-surface electrical conduction in porous media, *Physical Review B*, **55**(3), 1757-1773, doi:10.1103/PhysRevB.55.1757.

Revil, A. & Leroy, P., 2001. Hydroelectric coupling in a Clayey Material, *Geophysical Research Letters*, **28**(8), 1643-1646, doi:10.1029/2000GL012268.

Revil, A. & Leroy, P., 2004. Constitutive equations for ionic transport in porous shales, *Journal of Geophysical Research - Solid Earth*, **109**, B03208, doi:10.1029/2003jb002755.

Revil, A., Leroy, P. & Titov, K., 2005. Characterization of transport properties of argillaceous sediments: Application to the Callovo-Oxfordian argillite, *Journal of Geophysical Research - Solid Earth*, **110**, B06202, doi:10.1029/2004jb003442.

Rotenberg, B., Cadéne, A., Dufrêche, J. F., Durand-Vidal, S., Badot, J. C. & Turq, P., 2005. An Analytical Model for Probing Ion Dynamics in Clays with Broadband Dielectric

Spectroscopy, *The Journal of Physical Chemistry B,* **109,** 15548-15557, doi:10.1021/jp051586k.
Rotenberg, B., Marry, V., Dufreche, J. F., Malikova, N., Giffaut, E. & Turq, P., 2007. Modelling water and ion diffusion in clays: A multiscale approach, *Comptes Rendus Chimie,* **10,** 1108-1116, doi:10.1016/j.crci.2007.02.009.
Sahai, N. & Sverjensky, D. A., 1997. Evaluation of internally consistent parameters for the triple-layer model by the systematic analysis of oxide surface titration data, *Geochimica et Cosmochimica Acta*, **61**(14), 2801-2826, doi:10.1016/S0016-7037(97)00128-2.
Schramm, L. L. & Kwak, J. C. T., 1982. Influence of Exchangeable Cation Composition on the Size and Shape of Montmorillonite Particles in Dilute Suspension, *Clays and Clay Minerals*, **30**(1), 40-48, doi:10.1346/Ccmn.1982.0300105.
Schroeder, P. A., 2018. Clays in the Critical Zone, Cambridge University Press, Cambridge, UK, 254 pp., doi:10.1017/9781316480083.
Schwarz, G., 1962. A theory of the low-frequency dielectric dispersion of colloidal particles in electrolyte solution, *The Journal of Physical Chemistry*, **66**, 2636-2642, doi:10.1021/j100818a067
Sen, P. N., 1984. Grain Shape Effects on Dielectric and Electrical-Properties of Rocks, *Geophysics*, **49**(5), 586-587, doi:10.1190/1.1441695.
Shim, Y.-S., Kim, Y.-K., Kong, S.-H., Rhee, S.-W. & Lee, W.-K., 2003. The adsorption characteristics of heavy metals by various particle sizes of MSWI bottom ash, *Waste Management*, **23**(9), 851-857, doi:10.1016/s0956-053x(02)00163-0.
Sposito, G., 1989. The Chemistry of Soils, Oxford University Press, New York, 344 pp.
Tao, H., Qian, X., Zhou, Y. & Cheng, H., 2022. Research progress of clay minerals in carbon dioxide capture, *Renewable and Sustainable Energy Reviews*, **164**, 112536, doi:10.1016/j.rser.2022.112536.
Thiry, M., 2000. Palaeoclimatic interpretation of clay minerals in marine deposits: an outlook from the continental origin, *Earth-Science Reviews*, **49**(1-4), 201-221, doi:10.1016/s0012-8252(99)00054-9.
Tinnacher, R. M., Holmboe, M., Tournassat, C., Bourg, I. C. & Davis, J. A., 2016. Ion adsorption and diffusion in smectite: Molecular, pore, and continuum scale views, *Geochimica et Cosmochimica Acta*, **177**, 130-149, doi:10.1016/j.gca.2015.12.010.
Tombacz, E. & Szekeres, M., 2004. Colloidal behavior of aqueous montmorillonite suspensions: the specific role of pH in the presence of indifferent electrolytes, *Applied Clay Science*, **27**(1-2), 75-94, doi:10.1016/j.clay.2004.01.001.
Tombacz, E. & Szekeres, M., 2006. Surface charge heterogeneity of kaolinite in aqueous suspension in comparison with montmorillonite, *Applied Clay Science*, **34**(1-4), 105-124, doi:10.1016/j.clay.2006.05.009.
Tournassat, C., Neaman, A., Villieras, F., Bosbach, D. & Charlet, L., 2003. Nanomorphology of montmorillonite particles: Estimation of the clay edge sorption site density by low-pressure gas adsorption and AFM observations, *American Mineralogist,* **88,** 1989-1995, doi:10.2138/am-2003-11-1243.
Tournassat, C. & Appelo, C. A. J., 2011. Modelling approaches for anion-exclusion in compacted Na-bentonite, *Geochimica et Cosmochimica Acta*, **75**(13), 3698-3710, doi:10.1016/j.gca.2011.04.001.
Tournassat, C., Bizi, M., Braibant, G. & Crouzet, C., 2011. Influence of montmorillonite tactoid size on Na-Ca cation exchange reactions, *Journal of Colloid and Interface Science*, **364**(2), 443-454, doi:10.1016/j.jcis.2011.07.039.
Tournassat, C., Bourg, I. C., Steefel, C. I. & Bergaya, F., 2015. Surface Properties of Clay Minerals, in: *Developments in Clay Science*, 6, edited by Tournassat, C., Steefel, C. I., Bourg, I. C. & Bergaya, F., pp. 5-31, Elsevier, doi:10.1016/b978-0-08-100027-4.00001-

2.
Tournassat, C., Chapron, Y., Leroy, P., Bizi, M. & Boulahya, F., 2009. Comparison of molecular dynamics simulations with triple layer and modified Gouy-Chapman models in a 0.1 M NaCl-montmorillonite system, *Journal of Colloid and Interface Science*, **339**(2), 533-541, doi:10.1016/j.jcis.2009.06.051.
Tournassat, C., Gaboreau, S., Robinet, J. C., Bourg, I. & Steefel, C. I., 2016. Impact of microstructure on anion exclusion in compacted clay media, **22,** 137-149, doi:10.1346/cms-wls-21.11.
Tournassat, C. & Steefel, C. I., 2019. Reactive Transport Modeling of Coupled Processes in Nanoporous Media, *Reviews in Mineralogy and Geochemistry*, **85**(1), 75-109, doi:10.2138/rmg.2019.85.4.
Ural, N., 2018. Chapter 5 The Importance of Clay in Geotechnical Engineering. in Current Topics in the Utilization of Clay in Industrial and Medical Applications, doi:10.5772/intechopen.75817.
Vinegar, H. J. & Waxman, M. H., 1984. Induced Polarization of Shaly Sands, *Geophysics*, **49**(8), 1267-1287, doi:10.1190/1.1441755.
Weller, A., Slater, L. & Nordsiek, S., 2013. On the relationship between induced polarization and surface conductivity: Implications for petrophysical interpretation of electrical measurements, *Geophysics*, **78**(5), D315-D325, doi:10.1190/Geo2013-0076.1.
Yven, B., Sammartino, S., Géraud, Y., Homand, F. & Villieras, F., 2007. Mineralogy, texture and porosity of Callovo-Oxfordian argillite of the Meuse/Haute-Marne region, eastern Paris Basin, *Mémoires de la Société Géologique de France*, **178**, 73-90.
Zhou, Z. & Gunter, W. D., 1992. The Nature of the Surface Charge of Kaolinite, *Clays and Clay Minerals,* **40,** 365-368, doi:10.1346/ccmn.1992.0400320.

APPENDIX A. COMPUTATION OF THE DEBYE DECOMPOSITION

Following the Debye decomposition, the complex conductivity σ^* can be written as:

$$\sigma^*(\omega_k) = \sigma_\infty + (\sigma_0 - \sigma_\infty) \sum_{j=1}^{N_\tau} \frac{m_j}{1 + i\omega_k \tau_j} + i\omega_k C, \tag{A1}$$

where σ_∞ is the limit value of $|\sigma^*|$ at "infinite" frequency, σ_0 is the limit value of $|\sigma^*|$ at zero frequency, $\omega_k = 2\pi f_k$ is the k^{th} pulsation or angular frequency with f_k, $k = 1 \ldots N_f$, being the frequencies at which the measurements were done, τ_j, $j = 1 \ldots N_\tau$, are the relaxation times, and m_j, $j = 1 \ldots N_\tau$, is the partial chargeability distribution. The last term in Eq. A1 was introduced to take into account the high-frequency trend of the spectrum (see Florsch *et al.* 2014), due to Maxwell-Wagner polarisation, and/or contact impedance of the potential electrodes, and/or electromagnetic coupling effects between acquisition cables.

We chose the τ_j, $j = 1 \ldots N_\tau$, values in such a way that N_τ is less than $N_f / 2$ and that the number of points per decade is an entire number. The τ_j values are logarithmically distributed between $\tau_{\min}$ and $\tau_{\max}$, with

$$\begin{cases} \tau_{\min} = 10^{\left\lfloor \log_{10}\left(\frac{1}{2\pi f_{N_f}}\right) \right\rfloor} \\ \tau_{\max} = 10^{\left\lceil \log_{10}\left(\frac{1}{2\pi f_1}\right) \right\rceil} \end{cases}. \tag{A2}$$

Using a simulated annealing procedure (see Maineult 2016) we searched for σ_∞, m_j (for $j = 1 \ldots N_\tau$) and C. This approach supposes that σ_0 is known, since the term $(\sigma_0 - \sigma_\infty)$ cannot be separated from the m terms in practice. To determine the value of σ_0, we first fitted the measured spectra with a double Cole-Cole model:

$$\sigma^*(\omega) = \sigma_0 \left[1 + \frac{m_{CC,1}}{1 - m_{CC,1}} \left(1 - \frac{1}{1 + \left(i\omega\tau_{CC,1} \right)^{c_{CC,1}}} \right) + \frac{m_{CC,2}}{1 - m_{CC,2}} \left(1 - \frac{1}{1 + \left(i\omega\tau_{CC,2} \right)^{c_{CC,2}}} \right) \right] + i\omega C_{CC}, \quad \text{(A3)}$$

using the simplex algorithm to search for σ_0, $m_{CC,1}$, $m_{CC,2}$ (the chargeabilities associated with the first and second peak, respectively), $\tau_{CC,1}$, $\tau_{CC,2}$ (the associated relaxation times), $c_{CC,1}$, $c_{CC,2}$ (the associated Cole-Cole exponents) and C_{CC}. We then injected the value of σ_0 into the simulated annealing procedure.

APPENDIX B. CORRECTION OF THE CONTACT IMPEDANCE AND ELECTROMAGNETIC COUPLING EFFECTS ON THE MEASURED SIP DATA

Tables B1 shows the values of the coupling coefficient C_c computed to remove the contact impedance and electromagnetic coupling effects from the complex conductivity measurements.

Table B1. Contact impedance and electromagnetic coupling effects correction of the SIP measurements

Clays	Kaol.	Kaol.	Illite	Illite	G. Mt	G. Mt	R. Mt	R. Mt	R. Mt
C_b (M)	0.0154	0.1908	0.0180	0.1816	0.0153	0.1457	0.0171	0.1541	1.5091
$\log C_c$	-7.874	-7.372	-7.863	-7.642	-7.322	-6.949	-7.141	-7.000	-8.072